Deep Understanding of Strong Metal Interface Confinement: A Journey of Pd/FeO_x Catalysts

Jixing Liu, Lu Wang, Francis Okejiri, Jing Luo, Jiahua Zhao, Pengfei Zhang,* Miaomiao Liu, Shize Yang,Zihao Zhang, Weiyu Song, Wenshuai Zhu, Jian Liu,* Zhen Zhao, Guodong Feng,* Chunming Xu, and Sheng Dai*

Abstract

Tuning the atomic interface configuration of noble metals (NMs) and transition-metal oxides is an effective straightforward yet challenging strategy to modulate the activity and stability of heterogeneous catalysts. Herein, Pd supported on mesoporous Fe_2O_3 with a high specific surface area was rationally designed and chosen to construct the Pd/iron oxide interface. As a versatile model, the physicochemical environments of Pd nanoparticles (NPs) could be precisely controlled by taming the reduction temperature. The experimental and density functional theory calculation results unveiled that the catalyst in the support− metal interface confinement (SMIC) state showed significantly enhanced catalytic activity and sintering resistance for CO oxidation. The constructed Fe sites at the interfaces between FeO_x overlayers and Pd NPs not only provided additional coordinative unsaturated ferrous sites for the adsorption and activation of O_2, thereby facilitating the activation efficiency of O_2, but also impressively changed the reaction pathway of CO oxidation. As a result, the catalyst followed the Pd/Fe dual-site mechanism instead of the classical Mars−van Krevelen mechanism. For the catalyst in the strong metal−support interaction (SMSI) state, its catalytic activity was seriously suppressed because of the excessive encapsulation of the active Pd sites by FeO_x overlayers. The present study therefore provides detailed insights into the SMIC and SMSI in ferric oxide-supported Pd catalysts, which could guide the preparation of highly efficient supported catalysts for practical applications.

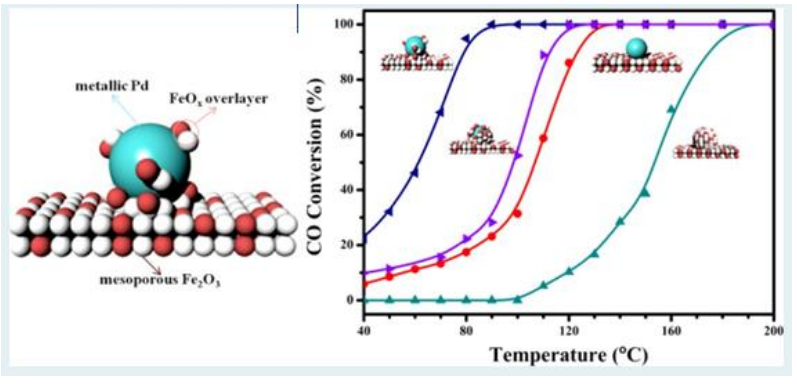

Keywords

FeO_x overlayers, Pd, interface, support−metal interface confinement, density functional theory

Acknowledgments

S.D., M.L., Z.Z., and F.O. were supported by the U.S. Department of Energy, Office of Science, Office of Basic Energy Sciences, Chemical Sciences, Geosciences, and Biosciences Division, Catalysis Science program. Jixing Liu and Jing Luo thank the National Natural Science Foundation of China (21673290, U1662103). P.Z. acknowledges the National Natural Science Foundation of China (grant no. 21776174), the Thousand Talents Program, the Open Foundation of the State Key Laboratory of Ocean Engineering (Shanghai Jiao Tong University of China) (no. 1809), Shanghai Jiao Tong University Scientific and Technological Innovation Funds, the China Shipbuilding Industry Corpo- ration and Zhejiang Xinan Chemical Industrial Group for their support. G.F. was supported by the National Natural Science Foundation of China (nos. 21871007, 21801009); the Natural Science Foundation of Shaanxi Province (nos. 2019JLM-15, 2018JM2006).

Introduction

Noble metals (NMs) supported on transition-metal oxides (TMOs) with high specific surface areas have received increasing attention on account of their outstanding perform- ances in heterogeneous catalysis.[1−16] The interaction of NMs with TMOs, especially reducible oxides (e.g., FeO_x, CeO_2, and TiO_2), has been generally defined as strong metal−support interaction (SMSI),[17−22] and it plays a crucial role in improving the NM's sintering resistance by encapsulation of NMs with reducible TMO overlayers. The interface induced by SMSI is found to significantly influence the catalytic activity for CO oxidation because of the creation of rich oxide edge sites,[23−25] speci*fi*cally coordinative unsaturated sites (CUSs). Two different states can be achieved via tailoring post-treatment conditions. For the catalyst in the SMSI state proposed by Tauster et al.,[26] the catalytic activity for CO oxidation is generally inhibited because the NM surfaces are almost fully encapsulated by TMO overlayers, resulting in the blockage of active NM sites despite abundant CUSs.[27] In sharp contrast, for the catalyst in the support−metal interface confinement (SMIC) state introduced by Zhang and Fu,[28] oxide overlayers are deliberately constructed on NM surfaces to produce highly dispersed two-dimensional oxide nanostructures and create high density CUSs between the interfaces of NMs and TMO overlayers. The catalytic activity for CO oxidation is thereafter promoted. How these highly active sites facilitate the catalytic activity during CO oxidation, however, remains a matter of debate.

In this regard, Fu and co-workers conducted extensive work and highlighted that Pt/FeO_x catalyst pretreated in air at high temperatures ($500 < t < 800$ °C) can form the SMIC state.[29] This structure not only significantly improved O_2 activation but also promoted the formation of atomic oxygen species, followed by reaction with CO adsorbed on Pt surface sites nearby through the Langmuir−Hinshelwood (LH) mechanism. The catalytic performance of this Pt/FeO_x catalyst therefore was enhanced. In contrast, the Pt/FeO_x catalyst pretreated in air at 900 °C exhibited sharply suppressed CO oxidation activity because of the complete encapsulation of the metal active sites in the SMSI state.[27] Nevertheless, Xiao et al. developed a wet chemical (wc) strategy to prepare Au/TiO_2- wcSMSI, which demonstrated improved CO oxidation activity because of the interface effect between Au nanoparticles (NPs) and TiO_x overlayers.[22] It has been recognized that the support considerably influences the catalytic activities of TMO-supported NM catalysts for CO oxidation[30−32] and that NMs/TMOs generally follow two mechanisms-LH and Mars−van Krevelen (M−vK) mechanisms.[33] The former mechanism involves direct reaction of CO with adsorbed atomic oxygen species; on the other hand, the latter mechanism starts with the transfer of O atoms to CO, inducing oxygen vacancies on TMOs. To date, however, a general consensus on the role of overlayers on the effect of catalytic activity and reaction mechanism of NMs/TMOs for CO oxidation has not been reached yet.

In fact, various strategies have been adopted to tailor the atomic-scale interfacial structure and chemical state between NMs and TMOs.[22,29,34,35] However, previous works somewhat lack detailed investigations of morphological evolution with the change in treatment conditions. As a result, it remains unclear how the atomic-scale structure and chemistry of interface evolution in such catalyst systems influence the catalytic mechanism. In the present study, mesoporous Pd/Fe_2O_3 was chosen to construct the NM/iron oxide interface, which naturally provided both SMIC and SMSI states by taming the reduction temperature. The catalyst in the SMIC state obtained by treating fresh Pd/Fe_2O_3 at relatively lower reduction temperatures (50 or 100 °C) considerably improved its catalytic activity and sintering resistance. The emerging Fe sites at FeO_x/Pd interfaces, which are coordinative unsaturated Fe (CUF) sites, provided new adsorption and activation sites for O_2, facilitating the activation e*ffi*ciency of O_2. The reaction pathway of CO oxidation on Pd/Fe_2O_3 catalyst in the SMIC state thereafter was altered, in accordance with the Pd/Fe dual- site mechanism instead of the M−vK mechanism. For the catalyst in the SMSI state obtained by reducing the sample at higher temperatures (>200 °C), the catalytic activity was seriously inhibited because the active Pd sites were almost obstructed by the overlayers. This work presents a deep understanding of SMIC and SMSI in ferric oxide-supported Pdcatalysts.

Methods

Catalyst Synthesis.

Preparation of Fe_2O_3: The Fe_2O_3 support with a high specific surface area was fabricated by an aluminum hydroxide-mediated mechanochemical nanocasting strategy.[36] $Fe(NO_3)_3 \cdot 9H_2O$ (1.00 g) and aluminum hydroxide (1.00 g) were introduced into a 25 mL zirconia reactor containing four zirconia ball bearings (diameter 4 × 1.0 cm; total mass 8.6 g). Subsequently, the reactor was ball-milled for 1 h in a high-speed vibrating ball miller with a vibrational frequency of 30 Hz. The final products were obtained after being calcined (400 °C, 3 h), washed with 1 M NaOH solutionat 60 °C, and followed by being dried at 100 °C for overnight.

Preparation of Pd/Fe_2O_3: Pd NPs were synthesized according to a typical method: under gentle nitrogen flow, 0.20 g of borane−morpholine complex (1.9 mmol, Sigma- Aldrich 95%) and 10 mL of oleylamine (OAm, Acros 80−90%) were introduced into a four-necked glass reactor and then magnetically stirred and heated to 75 °C. Subsequently, a palladium solution containing 0.07 g of palladium(II) acetylacetonate ($Pd(acac)_2$, 0.23 mmol, Sigma-Aldrich 99%)m and 4.0 mL of OAm were injected into the above solution. After being stirred at this temperature for 1 h, the obtained solution was heated to 220 °C and kept for another 30 min before it was cooled down to 70 °C. The resulting NPs were obtained by addition of isopropanol (40 mL), centrifugation (8500 rpm, 10 min), dispersion in hexane (15 mL), and followed by centrifugation (9000 rpm, 12 min) after addition of ethanol (35 mL).

Pd/Fe_2O_3 was prepared by a facile adsorption method. Typically, 0.20 g of Fe_2O_3 powder was well dispersed in 20 mL of hexane solution with rigorous stirring. Next, the above as- prepared Pd NPs were dispersed in 10 mL of hexane and then were added dropwise into Fe_2O_3 solution under stirring. After continuing stirring for 12 h and followed by aging for another 12 h, the solution was centrifugated and washed with deionized water and ethanol three times and dried at 60 °C in air overnight. The final catalyst was obtained by being annealed for 3 h at 400 °C in air and denoted as Pd/Fe_2O_3-air. Pd/Fe_2O_3-H_2-*X* catalysts were achieved by treating the Pd/Fe_2O_3- air sample at the desired temperature (*X* = 50, 100, 200, and 400 °C) in H_2/N_2 for 1 h.

Catalyst Characterization.

The microstructure of Pd/Fe_2O_3 catalysts was observed by high-angle annular dark-field scanning transmission electron microscopy (HAADF- STEM) and high-resolution HAADF-STEM. The pore structure of Pd/Fe_2O_3 catalysts was analyzed by the adsorption branch of the nitrogen adsorption isotherm recorded at 77 K via a Gemini VII surface area analyzer. The phase composition of Pd/Fe_2O_3 samples was characterized by the X-ray diffraction (XRD) pattern in a 2θ interval of 10−80°. The chemical state of iron species over Pd/Fe_2O_3 samples was probed by X-ray photoelectron spectra (XPS) and X-ray absorption near-edge structure (XANES) spectra.

Catalytic CO Oxidation.

The catalytic activities of as-prepared metal oxides for CO oxidation were evaluated in a continuous-flow reactor equipped with a straight quartz glass tube at atmospheric pressure. The feeding gas of 1% CO flow balanced with dry air was passed through the catalyst bed at a gas hourly space velocity (GHSV) of 30,000 $mL \cdot g_{cat}^{-1} \cdot h^{-1}$. The gas was monitored by Horiba S4932/MT, and the reaction temperature was adjusted from room temperature to the temperature of complete CO conversion. The CO concentration was determined using an on-line gas chromato- graph (Buck Scientific 910). The CO conversion was calculated based on the content change of CO in feed gasand an effluent stream.

Results and Discussion

Synthesis and Structural Characterization of Pd/Fe_3O_3 Catalysts.

Mesoporous Fe_2O_3 was fabricated by an aluminum hydroxide-mediated mechanochemical nanocasting strategy (Figure 1). Initially, ferric nitrate and aluminum hydroxide may undergo solid transfer to form a uniform distribution of iron salts on a porous aluminum matrix. After calcination and removal of Al species, a mesoporous Fe_2O_3 network was released. On the basis of mesoporous Fe_2O_3 support, Pd NPs were loaded by

the adsorption method, and the actual Pd loading amount determined by inductively coupled plasma atomic emission spectroscopy was 1.2 wt %. Finally, by simply regulating the reduction temperature, the states (SMIC and SMSI) of Pd/Fe_2O_3 could be precisely controlled. Their morphologies and catalytic activities there- fore could be modulated.

The morphology of the mesoporous Fe_2O_3 sample was first observed by HAADF-STEM. The Fe_2O_3 support showed a sponge like nanoarchitecture that was composed of interstitial porosity with pore sizes ranging from 3 to 6 nm (Figure 2a). The pore property of Fe_2O_3 support was further characterized by N_2 adsorption measurement at 77 K. Fe_2O_3 displayed a typical type-IV curve and pore size distribution centered at ∼4.1 nm, demonstrating its mesoporous structure (Figure 2b). Subsequently, HAADF-STEM was employed to analyze Fe_2O_3-loaded Pd NPs, and it was noted that the particle size distribution of as-prepared Pd NPs ranged from 2 to 4 nm (Figure S2). Moreover, the loading of Pd NPs did not severely influence the porous structure of the Fe_2O_3 support (Figure 2c), which was consistent with the results of N_2 adsorption isotherm and pore size distribution of Pd/Fe_2O_3 (Figure 2b). The high-resolution HAADF-STEM (Figure 2d) image of the Pd/Fe_2O_3-air catalyst evidenced a ∼3 nm metallic Pd NP supported on Fe_2O_3 with a visible *d*-spacing of the Fe_2O_3(006) plane of 0.229 nm.

Insights into the Morphological Evolution of Pd/Fe_2O_3 Catalysts.

HAADF-STEM images and elemental mapping *fi*gures were further collected to explore the effect of H_2 treatment on Pd/Fe_2O_3 samples. Figure 3a shows the Pd/Fe_2O_3-H_2-100 sample, which was obtained after the post- treatment of Pd/Fe_2O_3 in H_2 at 100 °C. Figure 3a_2 con*fi*rmed that the lattice spacing of 0.225 nm was well in accordance with the (111) crystal plane of Pd NPs. Elemental mapping analyses revealed that only very few Pd NPs stood on the surface of Fe_2O_3 support. As the reduction temperature was increased from 200 °C (Figure 3b_1−b_5) to 400 °C (Figure 3c_1−c_5), no evident variation in the particle size distribution of Pd NPs was noted (Figure S3), while the Pd NP surfaces of Pd/Fe_2O_3 were gradually covered by FeO_x species. This coverage was strongly associated with strong metal (Pd)− support (Fe_2O_3) interaction, and the temperature-directed morphological evolution can be narrated in Figure 1. From another perspective, when the surfaces of Pd NPs were completely covered by FeO_x species, the active sites were then blocked, which may be unfavorable for the catalytic reaction.

Figure S4 depicts the XRD patterns of Fe_2O_3, Pd/Fe_2O_3, and Pd/Fe_2O_3 catalysts treated in H_2 flow from 50 to 400 °C. The oxide support was comprised of a pure Fe_2O_3 phase (Figure S4a), and the distinct diffraction peaks of Pd/Fe_2O_3 (Figure S4b) matched well with that of pristine Fe_2O_3. The absence of diffraction peaks for Pd species suggested the high dispersion of Pd species. The peaks of Pd/Fe_2O_3 at 24.1, 33.2, 35.6, 39.3, 40.9, 49.5, 54.1, 57.4, 64.0, and 66.0° corresponded to the (012), (104), (110), (006), (200), (113), (024), (116), (122), (300), and (125) crystal planes of hexa-Fe_2O_3 (PDF#33-0664), respectively.[37] Even though the Pd/Fe_2O_3 sample was treated in H_2 at relatively low temperatures (≤200 °C), no other crystalline phase reflections were detected. Nevertheless, when the reduction temperature was elevated to 400 °C, characteristic peaks corresponding to the Fe_3O_4 crystalline phase (PDF#19-0629) were detected at 30.1, 35.4, and 43.1°, which could be assigned to the (220), (311), and (400) crystal planes, respectively.[38,39] Thus, it indicated that a portion of the Fe^{3+} species was reduced to Fe^{2+} species.

Atomic Structure Analysis of Pd/Fe2O3 Catalysts by XPS and XANES.

XPS and X-ray XANES spectrum analyses were further conducted to probe the effect of H_2 treatment on the chemical state of interface Pd/iron species. Figure 4A illustrates the Pd 3d XPS of Pd/Fe_2O_3 samples. Both the bands at 335.5 and 340.8 eV were assigned to metallic Pd,[40,41] and these peaks gradually shifted to the higher binding energy with elevating reduction temperatures, thereby revealing the presence of strong electron transfer from metallic Pd to the FeO_x overlayers. This blue shift should be in turn favorable to weaken the CO adsorption and make CO more active toward the p electrons of dissociated oxygen, thereafter facilitating the catalytic performances of Pd/Fe_2O_3 samples for CO oxidation.[35,42,43] Figure 4B depicts that Fe 2p XPS of Pd/ Fe_2O_3 samples gradually moved to the lower binding energy with increasing reduction temperatures. To strikingly observe the variation of surface Fe species on Pd/Fe_2O_3 samples with the elevated reduction temperatures, we *fi*tted the corresponding Fe 2p XPS peaks at 709.3 and 711 eV, which were ascribed to the Fe^{2+} and Fe^{3+} species (Figure S5).[28] The surface relative concentration ratios of Fe^{3+} calculated from the peak fitting of Fe 2p XPS are

summarized in Table S1. With the increasing of reduction temperatures, the surface relative concentration ratio of Fe^{3+} markedly declined, especially for the Pd/Fe_2O_3-H_2-400 sample. This result suggested the reduction of iron species over Pd/Fe_2O_3 samples at high reduction temperatures, in agree- ment with the observation in XRD. Figure 4C,D exhibits the Pd L-edge and Fe K-edge XANES spectra of Pd/Fe_2O_3 samples, respectively. The intensities of the adsorption peaks (Figure 4C) notably increased with elevating reduction temperature, while almost no changes occurred in the peak position. It has been identified that the intensity of the white line at the L-edge represents the extent of reducibility for the absorbing atoms, and the position can reflect the variation in NM size.[44−46] A more intense white line of Pd species indicates a higher oxidation state,[46] collaborating the presence of electron-deficient Pd from XPS result. Almost no distinct position change after post-treatment implies no variation of the size of Pd NPs. This result was in full accordance with the high-resolution HAADF-STEM observations (Figure S3). Likewise, Fe K-edge XANES spectra demonstrated the red shift of Fe species, which may be due to the sintering of FeO_x resulting from high-temperature treatment. Therefore, based on the above results, it is plausible to exclude the effect of Pd NP size on the distinct variation of catalytic activity of Pd/Fe_2O_3 catalysts for CO oxidation.

Catalytic Performances for CO Oxidation.

Figure 5A shows the catalytic performances of various catalysts for CO oxidation, which decreased in the following sequence: Pd/Fe_2O_3-H_2-100 > Pd/Fe_2O_3-H_2-50 > Pd/Fe_2O_3-H_2-200 > Pd/Fe_2O_3-air > Pd/Fe_2O_3-H_2-400 > Fe_2O_3. As expected, Pd/Fe_2O_3-H_2-100 exhibited the highest catalytic activity with 100% CO conversion at 90 °C because of its optimal FeO_x overlayers on the Pd surfaces, which was more active than the Pd/Fe_2O_3-air catalyst with complete CO conversion at 140 °C. Notably, the catalytic activities of the Pd/Fe_2O_3 catalysts dramatically reduced with the treatment of high reduction temperatures, especially for Pd/Fe_2O_3-H_2-400 catalyst. The active Pd sites were completely coated and thereafter seriously obstructed by the outside FeO_x overlayers, thereby leading to an obvious decline in catalytic activity.

To further explore the morphology evolution of Pd/Fe_2O_3 catalysts for CO oxidation, we calculated the apparent activation energies (ΔE_a) under the exclusion of interparticle mass-transfer limitation (Figure S6). The structural state of Pd tremendously influences the ΔE_a of Pd/Fe_2O_3 catalysts (Figure 5B). The Pd/Fe_2O_3 catalyst in the SMSI state (Pd/Fe_2O_3-H_2-400) presents a pronouncedly higher ΔE_a value than those catalysts in the SMIC state (Pd/Fe_2O_3-H_2-X, $50 \leq X \leq 200$). The ΔE_a value declines in the following sequence: Pd/Fe_2O_3-H_2-400 (83.7 kJ/mol) > Pd/Fe_2O_3-air (61.5 kJ/mol) > Pd/Fe_2O_3-H_2-200 (51.6 kJ/mol) > Pd/Fe_2O_3-H_2-50 (44.2 kJ/mol) > Pd/Fe_2O_3-H_2-100 (33.6 kJ/mol), and Pd/Fe_2O_3-H_2- 100 exhibits the lowest activation energy possibly because of its optimal FeO_x overlayers on the Pd surfaces.

The sintering resistance of supported TMO catalysts actually is far from ideal.[47] Hence, the SMIC effect on the Pd/Fe_2O_3 stability for CO oxidation was further probed in the presence of H_2O and propene at 150 °C. Figure 5C illustrates that Pd/Fe_2O_3-air gave an initial CO conversion at 90.9%, which was almost similar to that of Pd/Fe_2O_3-H_2-100 (93.2%) at the beginning of the reaction. In contrast, the CO activity of Pd/Fe_2O_3-air decreased dramatically with the reaction time, achieving 70.7% after 24 h. In sharp contrast, Pd/Fe_2O_3-H_2- 100 underwent slow deactivation and still showed 87.2% CO conversion after the same reaction time. The chemical states of spent Pd/Fe_2O_3-air and Pd/Fe_2O_3-H_2-100 catalysts after reaction at 150 °C for 24 h were further detected by XPS spectra, thermogravimetric analysis (TGA), and HAADF- STEM (Figure S7). The observations showed that the deactivation of the Pd/Fe_2O_3-air catalyst should be reasonable because of the loss of active sites resulting from the sintering of Pd NPs (Figure S7C) rather than the oxidation of Pd (Figure S7A) and the buildup of carbonates (Figure S7B).[12,48] It also demonstrated that the signi*fi*cantly improved stability of Pd/Fe_2O_3-H_2-100 could be attributed to the protection of outside FeO_x overlayers, which greatly inhibited the sintering of Pd NPs.

DFT+ *U* Analyses.

To unveil the origin of enhanced catalytic activity for the Pd/Fe_2O_3 catalyst treated under low reduction temperatures (≤100 °C), we further carried out density functional theory (DFT) + U calculations. For CO oxidation by co-adsorbed O_2 on the Pd(111) surface: the Pd- only mechanism, the transition states (TSs), structures of intermediates, and relative energy diagram for CO oxidation over the Pd(111) surface are displayed in Figure S8. The adsorption and activation of O_2 on Pd surfaces were first considered, and the calculation

results are as follows. O_2 binds to the bridge site of Pd−Pd atoms with adsorption energy at −0.73 eV (IM1). The cleavage of O−O bond (O_2) results in the O−O bond length elongation from 1.33 Å (O_2 adsorption state) to 1.70 Å in the TS (TS1) with an oxygen dissociation barrier at 0.77 eV. O atoms are adsorbed on the hollow site between the three Pd atoms. There are two kinds of hollow sites on the Pd(111) surface, which are fcc (face-centered cubic) and hcp (hexagonal close-packed) sites, respectively. It has exothermic reaction energy at 1.42 eV when two O atoms are both adsorbed on the hcp hollow site. Based on the adsorption structure with two O atoms on the surface, we compared the pathway of CO oxidation following two possible configurations of CO adsorption on Pd sites. The adsorption of CO is easier to proceed via stabilization of C with three Pd atoms on the hollow site (IM3) compared with the bridge-site adsorption with two Pd atoms. The adsorbed CO thereafter combines with an adsorbed O atom on Pd to generate CO_2 (IM4) with exothermic reaction energy and activation barrier at 0.47 and 1.19 eV (TS2), respectively. Subsequently, CO_2 desorbs from the IM4 state with exothermic reaction energy of 0.35 eV. Finally, another CO adsorbs on the Pd(111) surface (IM6) followed by reacting with one O atom at the surface with an activation barrier at 1.18 eV (TS3) to form CO_2 with an exothermic reaction energy of 0.13 eV (IM7), and the desorption of CO_2 is also exothermic by 0.31 eV (FS). In addition to the adsorption of O on the hcp hollow site, two dissociated O atoms adsorbed on the fcc hollow site and two O atoms adsorbed on hcp and fcc hollow sites, respectively, were also studied. The results indicated that three reaction behaviors displayed similar energy and structure regardless of the types of O adsorption (Figures S9−S11).

Besides the adsorption on Pd surfaces, O_2 could also adsorb on Fe atoms at FeO_x/Pd interfaces, which could serve as alternative active binding sites. In this case, CO oxidation by O_2 adsorbed on the FeO_x/Pd(111) surface via the Pd/Fe dual-site mechanism, and this catalysis process follows the LH mechanism. As shown in Figure 6, the CUF site shows the strong ability for O_2 binding with an adsorption energy of −1.07 eV (IM1), and one O_2 could be easily split into two O atoms by elongation of the O−O bond length from 1.43 Å (IM1) in the O_2 adsorption state to 1.77 Å (TS1) with a dissociation barrier of 0.35 eV. These *f*indings coincide with the previous works that reported a similar activation barrier of 0.40 eV on FeO_x/Pt(111).[28,49] After O_2 dissociation, the exposed Fe site is then saturated by an adsorbed O atom with an exothermic reaction energy of 1.20 eV (IM2). For CO adsorption, CO preferentially adsorbs on a hollow site between three Pd atoms via a C atom with an exothermic energy of 2.50 eV (IM3). The CO molecule adsorbed on the fcc and hcp hollow sites were separately investigated, and no noticeable difference was found in their adsorption energies (Figures S9−S11). Subsequently, the adsorbed CO species combine with one O atom to form adsorbed CO_2 (IM4) with an endothermic reaction energy and activation barrier of 0.04 and 1.26 eV (TS2), respectively. Thereafter, the as-formed CO_2 desorbs from the FeO_x/Pd(111) surface with an exothermic reaction energy of 0.59 eV. Meanwhile, another adsorbed CO on Pd atoms of the FeO_x/Pd(111) surface (IM5) reacts with one O immobilized by Fe at the interface site with an activation barrier of 1.22 eV (TS3). The formation and desorption of CO_2 for this step are exothermic and endothermic by 0.53 and 0.10 eV, respectively.

In addition to the above-mentioned two possible reaction mechanisms, CO oxidation could also proceed via the M−vK mechanism by lattice oxygen on the FeO_x/Pd(111) surface (Figure S12). The catalytic process starts with CO adsorbed on Fe or Pd sites reacting with one lattice O atom at the interface of FeO_x, and there are two pathways for this transformation. The first pathway is CO adsorbing at the interface of the CUF site (IM1) with an exothermic reaction energy of 0.44 eV followed by reacting with one adjacent lattice O atom of FeO_x to produce CO_2 (IM2) with an endothermic reaction energy and activation barrier (TS1) of 0.17 and 1.22 eV, respectively. Subsequently, CO_2 desorption from the IM2 state induces the formation of an O vacancy on FeO_x with an exothermic reaction energy of 0.17 eV. One gaseous O_2 adsorbs on this O vacancy with an adsorption energy of −2.90 eV (IM4), accompanied by the scission of the O−O bond and subsequent redistribution of the O atom (IM5). The dissociated O stabilized on the CUF site (IM5) requires an exothermic reaction energy and activation barrier (TS2) of 1.98 and 0.78 eV, respectively. Thereafter, CO adsorption occurs on the hollow site with an adsorption energy of 0.77 eV (IM6), followed by reacting with one O atom adsorbed on the CUF site to generate CO_2 with an exothermic reaction energy and activation barrier of 0.53 eV (IM7) and 1.22 eV (TS3), respectively. Finally, CO_2 desorb from the IM7 state with a low desorption energy of 0.10 eV (FS). Another pathway is CO adsorbed on the hollow site between three Pd atoms of the FeO_x/Pd(111) surface (IM1*) with an exothermic reaction energy of 1.92 eV. The adsorbed CO reacts with one

neighboring lattice O atom of FeO_x to produce CO_2 (IM2*) with an activation barrier of 1.60 eV (TS1*) and an endothermic reaction energy of 1.03 eV. Subsequently, CO_2 desorption from the IM2* state gives rise to an O vacancy on FeO_x overlayers with a desorption energy of 0.45 eV (IM3), and the next steps are similar to those in the first pathway.

For the Pd-only mechanism, CO oxidation proceeds with CO and O_2 adsorbed on the Pd(111) surface. However, this inevitably results in the competitive adsorption behavior because of the fact that CO exhibits nearly two-fold adsorption capacity than O_2. Considering the energy of CO−metal surface interactions is distinctly higher than that of experimental values by Perdew−Burke−Ernzerhof (PBE) density functional, some- times by as much as 0.40 eV.[50−53] The activation energy barrier will be reduced to about 1 eV because the adsorption energy is overestimated. It is beneficial for the proceeding of reaction. However, the adsorption energy of CO on Pd is still higher than that of O_2 because of the high adsorption energy (>1 eV) of CO. This characteristic is unfavorable for the adsorption and activation of O_2, which can seriously affect the catalytic conversion efficiency of CO. A similar situation was also found in other NMs/TMO catalysts.[33,54] For CO oxidation on the FeO_x/Pd(111) surface, O_2 could adsorb on an alternative CUF site with higher adsorption energy than CO adsorbed on the CUF site. This scenario provides two adsorption sites including CUF and Pd(111) for realizing the co-adsorption of O_2 and CO. Thus, the *fi*rst pathway following the M−vK mechanism does not occur easily. For the Pd/Fe dual-site mechanism, the reaction of adsorbed CO on Pd(111) and O on Fe requires an activation energy of 1.26 eV, which is much lower than the calculated activation energy (1.60 eV) from the reaction of CO and lattice O. The above results demonstrate that CO oxidation on FeO_x/Pd is more likely to follow the Pd/Fe dual-site mechanism rather than the classical M−vK mechanism. Considering that the adsorption energy of CO is overestimated by PBE density functional,[50] the energy of the TS in the Pd/Fe dual-site mechanism will be reduced, which further promotes the occurrence of the reaction. More importantly, the FeO_x overlayers provide new CUF sites for the adsorption and activation of O_2, and the adsorption strength of O_2 on the CUF site is much higher than that of CO. In other words, O_2 and CO have their independent adsorption sites (CUF) on Pd(111). FeO_x/Pd(111) thereforeis more favorable for the CO oxidation reaction than Pd(111).

Conclusion

In summary, we designed mesoporous Fe_2O_3-supported Pd catalysts by a aluminum hydroxide-mediated mechanochemical nanocasting strategy. The effect of morphological evolution under different reduction temperatures on the catalytic activity and reaction mechanism over Pd/Fe_2O_3 was investigated by a combination of experiments and DFT calculations. The catalyst pretreated at low reduction temperatures resulted in Pd NP surfaces decorated by FeO_x overlayers (SMIC state). Further elevating the treatment temperature to 400 °C formed the SMSI state, in which Pd NPs were almost fully covered by FeO_x species. The catalyst in the SMIC state notably showed enhanced activity for CO oxidation compared to the pristine state because of the new CUF sites at the interfaces between FeO_x overlayers and Pd NPs. These CUF sites not only promoted the adsorption and activation of O_2, thereby facilitating the activation efficiency of O_2, but also changed the reaction pathway of CO oxidation. In contrast, the catalytic activity of the catalyst in the SMSI state was dramatically suppressed because the active Pd sites were completely covered by the surface FeO_x overlayers induced by the SMSI effect between metal and support. We believe that this work is favorable for the understanding of the SMIC and SMSI states in ferric oxide-supported Pd catalysts, which could guide the rational design of active-supported catalysts in the near future.

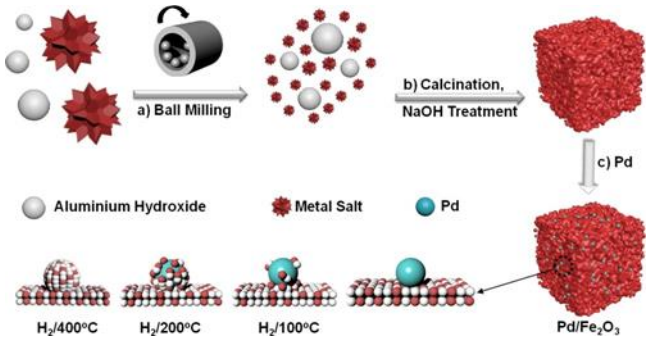

Figure 1. General $Al(OH)_3$-templated construction of mesoporous Pd/Fe_2O_3 catalyst and its morphological evolution in post-treatment.

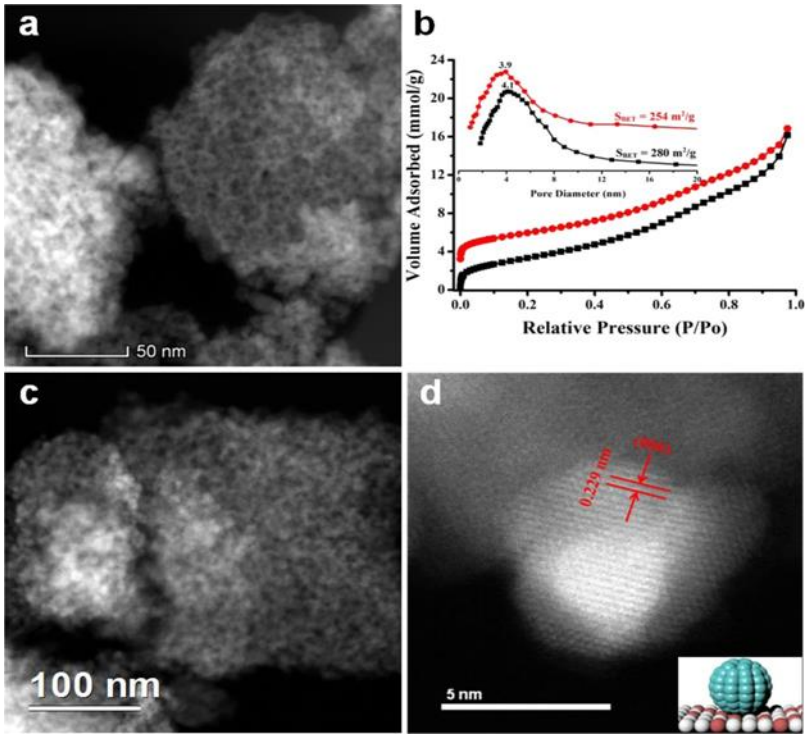

Figure 2. (a) HAADF-STEM image and (b) N_2 adsorption isotherm (77 K) and pore size distribution of Fe_2O_3 (black line) and Pd/Fe_2O_3 (redline), (c) HAADF-STEM, and (d) high-resolution HAADF-STEM images of Pd/Fe_2O_3-air.

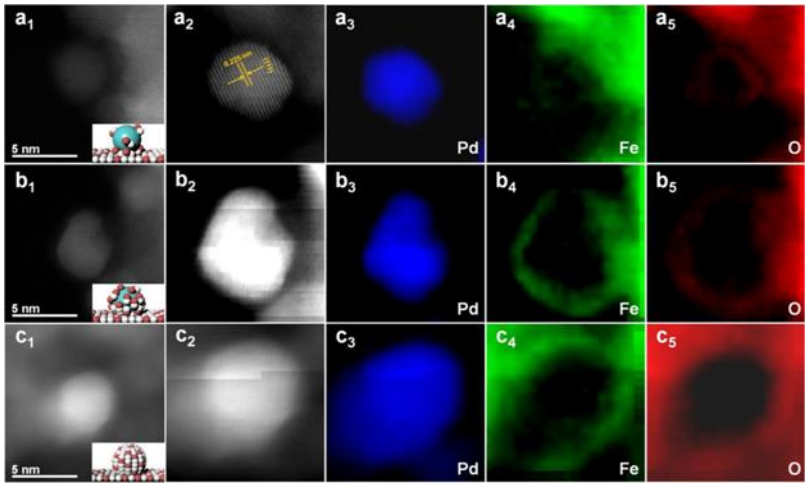

Figure 3. HAADF-STEM images and mapping elemental analyses for Pd/Fe_2O_3-H_2-100 (a_1-a_5), Pd/Fe_2O_3-H_2-200 (b_1-b_5), and Pd/Fe_2O_3-H_2-400 (c_1-c_5).

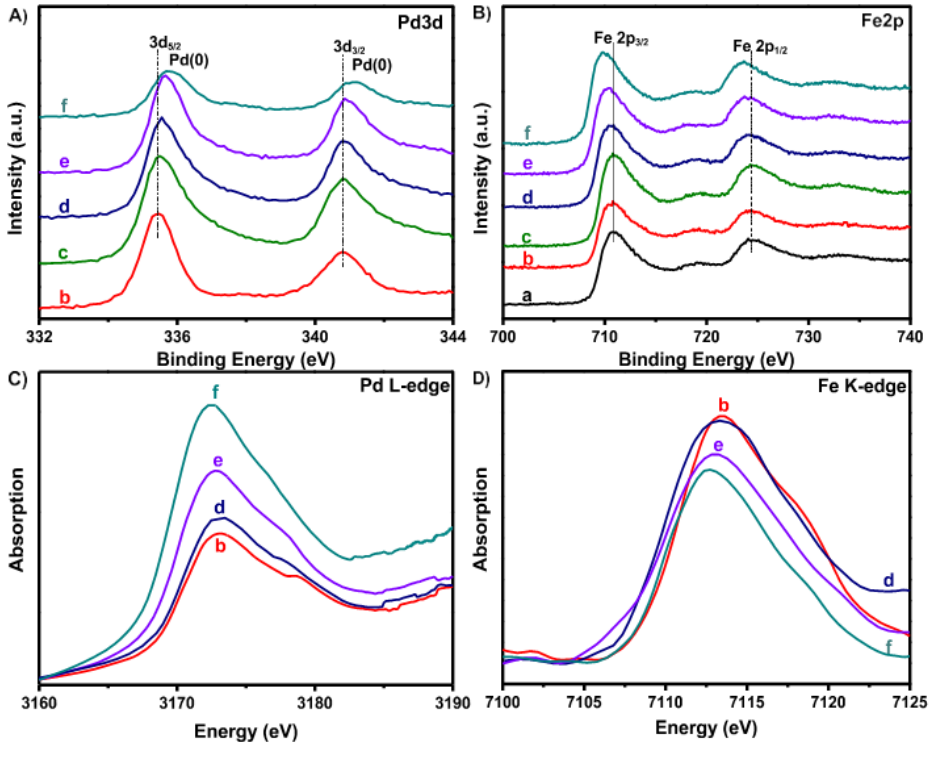

Figure 4. XPS of (A) Pd 3d and (B) Fe 2p and XANES spectra of (C) Pd L-edge and (D) Fe K-edge of the catalysts: (a) Fe_2O_3, (b) Pd/Fe_2O_3-air,(c) Pd/Fe_2O_3-H_2-50, (d) Pd/Fe_2O_3-H_2-100, (e) Pd/Fe_2O_3-H_2-200, and (f) Pd/Fe_2O_3-H_2-400.

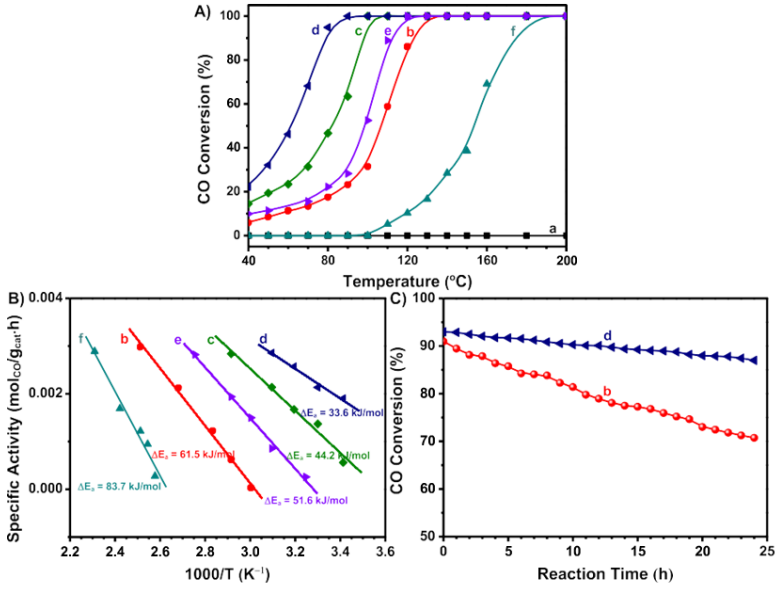

Figure 5. (A) CO conversion as a function of reaction temperature, the feed gas composition: 1.0 volume % CO balanced with dry air. The feed gas rate: 10 mL·min^{-1} and 20 mg of catalyst, corresponding to GHSV = 30,000 mL·(h·g$_{cat}$)$^{-1}$; (B) Arrhenius plots of CO conversion rates under CO conversions less than 10% over the catalysts: (a) Fe_2O_3, (b) Pd/Fe_2O_3-air, (c) Pd/Fe_2O_3-H_2-50, (d) Pd/Fe_2O_3-H_2-100, (e) Pd/Fe_2O_3-H_2-200, and (f) Pd/Fe_2O_3-H_2-400. Reaction mixtures contain 1.0 volume % CO balanced with dry air. The feed gas rate corresponded to GHSV = 360,000 mL· (h·g$_{cat}$)$^{-1}$. (C) CO conversion curves as a function of reaction time over (b) Pd/Fe_2O_3-air and (d) Pd/Fe_2O_3-H_2-100. The feed gas composition: 1.0 volume % CO, 0.01 volume % propene, 5 volume % H_2O balanced with dry air. The feed gas rate: 10 mL·min^{-1}, 20 mg of catalyst, and reaction temperature at 150 °C.

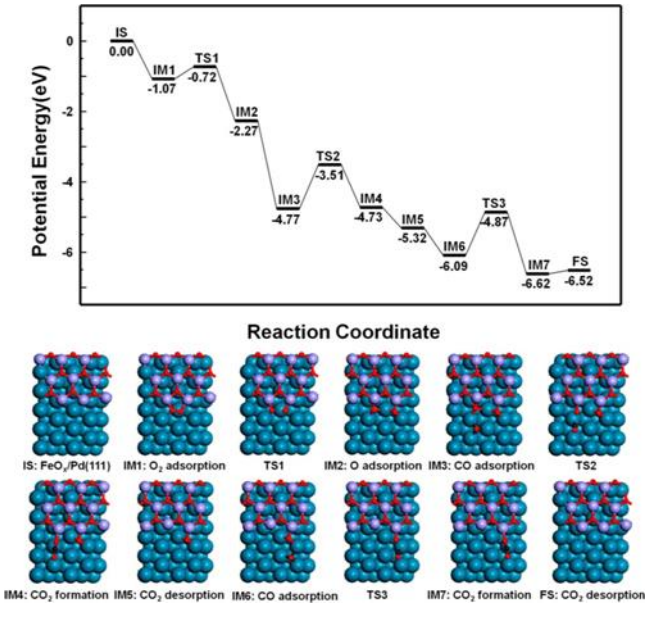

Figure 6. Potential energy diagram for CO oxidation on the FeO_x/ Pd(111) surface: Pd/Fe dual-site mechanism.

Author Information

Corresponding Authors:

Pengfei Zhang –
School of Chemistry and Chemical Engineering
Shanghai Jiao Tong University
Shanghai 200240,P. R. China

Jian Liu –
State Key Laboratory of Heavy Oil and Beijing KeyLab of Oil & Gas Pollution Control
China University of Petroleum
Beijing 102249, P. R. China

Guodong Feng –
Department of Chemistry
University of Tennessee−Knoxville
Knoxville, Tennessee 37996-1600, UnitedStates

Ningbo Institute of Materials Technology and Engineering
Chinese Academy of Sciences
Ningbo 315201, P.R. China

Key Laboratory of Advanced Molecular EngineeringMaterials
College of Chemistry and Chemical Engineering
Baoji University of Arts and Sciences
Baoji 721013, P. R. China

Sheng Dai –
Department of Chemistry
University of Tennessee−Knoxville
Knoxville, Tennessee 37996-1600, UnitedStates

Chemical Sciences Division,
Oak Ridge National Laboratory
Oak Ridge, Tennessee 37831, United States

Authors:
Jixing Liu –
School of Chemistry and Chemical Engineering
Institution for Energy Research
Jiangsu University, Zhenjiang 212013, P. R. China

State Key Laboratory of Heavy Oil andBeijing Key Lab of Oil & Gas Pollution Control
China University of Petroleum
Beijing 102249, P. R. China

Department of Chemistry
University of Tennessee−Knoxville
Knoxville, Tennessee 37996-1600, United States;

Lu Wang –
State Key Laboratory of Heavy Oil and Beijing KeyLab of Oil & Gas Pollution Control
China University of Petroleum
Beijing 102249, P. R. China

Francis Okejiri –
Department of Chemistry
University of Tennessee−Knoxville

Knoxville, Tennessee 37996-1600, UnitedStates

Jing Luo –
School of Chemistry and Chemical Engineering
Institution for Energy Research, Jiangsu University
Zhenjiang 212013, P. R. China

Jiahua Zhao –
School of Chemistry and Chemical Engineering,
Shanghai Jiao Tong University
Shanghai 200240, P. R. China

Miaomiao Liu –
Department of Chemistry
University of Tennessee−Knoxville, Knoxville
Tennessee 37996-1600, UnitedStates

Shize Yang –
Brookhaven National Laboratory
Upton, NewYork NY11973, United States

Zihao Zhang –
Department of Chemistry
University of Tennessee−Knoxville
Knoxville, Tennessee 37996-1600, UnitedStates

Weiyu Song –
State Key Laboratory of Heavy Oil and Beijing Key Lab of Oil & Gas Pollution Control
China University ofPetroleum,
Beijing 102249, P.R. China

Wenshuai Zhu –
School of Chemistry and Chemical Engineering
Institution for Energy Research
Jiangsu University
Zhenjiang 212013, P. R. China;

Zhen Zhao –
State Key Laboratory of Heavy Oil and Beijing Key Lab of Oil & Gas Pollution Control
China University of Petroleum
Beijing 102249, P. R. China

Chunming Xu –
State Key Laboratory of Heavy Oil and Beijing Key Lab of Oil & Gas Pollution Control
China University ofPetroleum
Beijing 102249, P. R. China

Author Contributions:

S.D. conceived the research idea. Jixing Liu, Jing Luo, Z.Z., C.X., and S.D. designed the experiments. Jixing Liu, Jing Luo, J.Z., M.L., P.Z., and F.O. performed all the experiments and analyzed all the data. S.Y. and G.F. conducted the STEM− HADDF images and XANES. L.W. and W.S. carried out the DFT calculations. All authors discussed the results and commented on the manuscript. Jixing Liu, P.Z., G.F., and S.D. cowrote the paper. Jixing Liu and L.W. contributed equally to this work.

References

(1) Rodriguez, J. A.; Grinter, D. C.; Liu, Z.; Palomino, R. M.; Senanayake, S. D. Ceria-based model catalysts: Fundamental studies on the importance of the metal−ceria interface in CO oxidation, the water−gas shift, CO_2 hydrogenation, and methane and alcohol reforming. Chem. Soc. Rev. 2017, 46, 1824−1841.

(2) Gerber, I. C.; Serp, P. A theory/experience description of support effects in carbon-supported catalysts. Chem. Rev. 2020, 120, 1250−1349.

(3) Wang, D.; Astruc, D. The recent development of efficient earth-abundant transition-metal nanocatalysts. Chem. Soc. Rev. 2017, 46, 816−854.

(4) Macino, M.; Barnes, A. J.; Althahban, S. M.; Qu, R.; Gibson, E. K.; Morgan, D. J.; Freakley, S. J.; Dimitratos, N.; Kiely, C. J.; Gao, X.; Beale, A. M.; Bethell, D.; He, Q.; Sankar, M.; Hutchings, G. J. Tuning of catalytic sites in Pt/TiO_2 catalysts for the chemoselective hydrogenation of 3-nitrostyrene. Nat. Catal. 2019, 2, 873−881.

(5) Pereira-Hernańdez, X. I.; DeLaRiva, A.; Muravev, V.; Kunwar, D.; Xiong, H.; Sudduth, B.; Engelhard, M.; Kovarik, L.; Hensen, E. J.; Wang, Y. Tuning $Pt-CeO_2$ interactions by high-temperature vapor- phase synthesis for improved reducibility of lattice oxygen. Nat. Commun. 2019, 10, 1358.

(6) DeRita, L.; Resasco, J.; Dai, S.; Boubnov, A.; Thang, H. V.; Hoffman, A. S.; Ro, I.; Graham, G. W.; Bare, S. R.; Pacchioni, G.; Pan, X.; Christopher, P. Structural evolution of atomically dispersed Pt catalysts dictates reactivity. Nat. Mater. 2019, 18, 746−751.

(7) Chen, A.; Yu, X.; Zhou, Y.; Miao, S.; Li, Y.; Kuld, S.; Sehested, J.; Liu, J.; Aoki, T.; Hong, S.; Camellone, M. F.; Fabris, S.; Ning, J.; Jin, C.; Yang, C.; Nefedov, A.; Wöll, C.; Wang, Y.; Shen, W. Structure of the catalytically active copper−ceria interfacial perimeter. Nat. Catal. 2019, 2, 334−341.

(8) Wang, L.; Wang, L.; Meng, X.; Xiao, F. S. New strategies for the preparation of sinter-resistant metal-nanoparticle-based catalysts. Adv. Mater. 2019, 31, 1901905.

(9) Yang, X.; Li, Q.; Lu, E.; Wang, Z.; Gong, X.; Yu, Z.; Guo, Y.; Wang, L.; Guo, Y.; Zhan, W. Taming the stability of Pd active phases through a compartmentalizing strategy toward nanostructured catalyst supports. Nat. Commun. 2019, 10, 1611.

(10) Li, W.; Zhang, G.; Jiang, X.; Liu, Y.; Zhu, J.; Ding, F.; Liu, Z.; Guo, X.; Song, C. CO2 Hydrogenation on unpromoted and M- promoted Co/TiO_2 catalysts (M = Zr, K, Cs): Effects of crystal phase of supports and metal−support interaction on tuning product distribution. ACS Catal. 2019, 9, 2739−2751.

(11) Therrien, A. J.; Hensley, A. J. R.; Marcinkowski, M. D.; Zhang, R.; Lucci, F. R.; Coughlin, B.; Schilling, A. C.; McEwen, J.-S.; Sykes, E. C. H. An atomic-scale view of single-site Pt catalysis for low- temperature CO oxidation. Nat. Catal. 2018, 1, 192−198.

(12) Matsubu, J. C.; Zhang, S.; DeRita, L.; Marinkovic, N. S.; Chen, J. G.; Graham, G. W.; Pan, X.; Christopher, P. Adsorbate-mediated strong metal−support interactions in oxide-supported Rh catalysts. Nat. Chem. 2017, 9, 120−127.

(13) Tang, H.; Su, Y.; Zhang, B.; Lee, A. F.; Isaacs, M. A.; Wilson, K.; Li, L.; Ren, Y.; Huang, J.; Haruta, M.; Qiao, B.; Liu, X.; Jin, C.; Su, D.; Wang, J.; Zhang, T. Classical strong metal−support interactions between gold nanoparticles and titanium dioxide. Sci. Adv. 2017, 3, No. e1700231.

(14) Wang, L.; Zhang, J.; Zhu, Y.; Xu, S.; Wang, C.; Bian, C.; Meng, X.; Xiao, F.-S. Strong metal−support interactions achieved by hydroxide-to-oxide support transformation for preparation of sinter- resistant gold nanoparticle catalysts. ACS Catal. 2017, 7, 7461−7465.

(15) Zhang, S.; Chang, C.-R.; Huang, Z.-Q.; Li, J.; Wu, Z.; Ma, Y.; Zhang, Z.; Wang, Y.; Qu, Y. High catalytic activity and chemo- selectivity of sub-nanometric Pd clusters on porous nanorods of CeO2 for hydrogenation of nitroarenes. J. Am. Chem. Soc. 2016, 138, 2629− 2637.

(16) Zhan, W.; He, Q.; Liu, X.; Guo, Y.; Wang, Y.; Wang, L.; Guo, Y.; Borisevich, A. Y.; Zhang, J.; Lu, G.; Dai, S. A sacrificial coating strategy toward enhancement of metal−support interaction for ultrastable Au nanocatalysts. J. Am. Chem. Soc. 2016, 138, 16130− 16139.

(17) Han, C. W.; Choksi, T.; Milligan, C.; Majumdar, P.; Manto, M.; Cui, Y.; Sang, X.; Unocic, R. R.; Zemlyanov, D.; Wang, C.; Ribeiro, F. H.; Greeley, J.; Ortalan, V. A discovery of strong metal-support bonding in nanoengineered $Au-Fe_3O_4$ dumbbell-like nanoparticles by in situ transmission electron microscopy. Nano Lett. 2017, 17, 4576− 4582.

(18) Merte, L. R.; Heard, C. J.; Zhang, F.; Choi, J.; Shipilin, M.; Gustafson, J.; Weaver, J. F.; Grönbeck, H.; Lundgren, E. Tuning the reactivity of ultrathin oxides: NO adsorption on monolayer FeO (111). Angew. Chem., Int. Ed. 2016, 55, 9267−9271.

(19) Carrasco, J.; Lopez-Duran, D.; Liu, Z.; Duchoň, T.; Evans, J.; Senanayake, S. D.; Crumlin, E. J.; Matolín, V.; Rodríguez, J. A.; Ganduglia-Pirovano, M. V. In situ and theoretical studies for the dissociation of water on an active Ni/CeO_2 catalyst: Importance of strong metal-support interactions for the cleavage of O-H Bonds. Angew. Chem., Int. Ed. 2015, 54, 3917−3921.

(20) Guo, Y.; Mei, S.; Yuan, K.; Wang, D.-J.; Liu, H.-C.; Yan, C.-H.; Zhang, Y.-W. Low-temperature CO2 methanation over CeO2- supported Ru single atoms, nanoclusters, and nanoparticles competitively tuned by strong metal-support interactions and h- spillover effect. ACS Catal. 2018, 8, 6203−6215.

(21) Bruix, A.; Rodriguez, J. A.; Ramírez, P. J.; Senanayake, S. D.; Evans, J.; Park, J. B.; Stacchiola, D.; Liu, P.; Hrbek, J.; Illas, F. A new type of strong metal−support interaction and the production of H_2 through the transformation of water on Pt/CeO_2 (111) and Pt/ CeOx/TiO2 (110) catalysts. J. Am. Chem. Soc. 2012, 134, 8968−8974.

(22) Zhang, J.; Wang, H.; Wang, L.; Ali, S.; Wang, C.; Wang, L.; Meng, X.; Li, B.; Su, D. S.; Xiao, F.-S. Wet-chemistry strong metal− support interactions in titania-supported Au catalysts. J. Am. Chem. Soc. 2019, 141, 2975−2983.
(23) Van Deelen, T. W.; Hernańdez Mejía, C.; de Jong, K. P. Control of metal-support interactions in heterogeneous catalysts to enhance activity and selectivity. Nat. Catal. 2019, 2, 955−970.
(24) Ro, I.; Resasco, J.; Christopher, P. Approaches for under- standing and controlling interfacial effects in oxide-supported metal catalysts. ACS Catal. 2018, 8, 7368−7387.
(25) Zhu, W.; Wu, Z.; Foo, G. S.; Gao, X.; Zhou, M.; Liu, B.; Veith, G. M.; Wu, P.; Browning, K. L.; Lee, H. N. Taming interfacial electronic properties of platinum nanoparticles on vacancy-abundant boron nitride nanosheets for enhanced catalysis. Nat. Commun. 2017, 8, 15291.
(26) Tauster, S. J.; Fung, S. C.; Garten, R. L. Strong metal-support interactions. Group 8 noble metals supported on titanium dioxide. J. Am. Chem. Soc. 1978, 100, 170−175.
(27) Xu, X.; Fu, Q.; Gan, L.; Zhu, J.; Bao, X. Interface-confined FeOx adlayers induced by metal support interaction in Pt/FeOx catalysts. J. Phys. Chem. B 2018, 122, 984−990.
(28) Fu, Q.; Li, W.-X.; Yao, Y.; Liu, H.; Su, H.-Y.; Ma, D.; Gu, X.-K.; Chen, L.; Wang, Z.; Zhang, H.; Wang, B.; Bao, X. Interface-confined ferrous centers for catalytic oxidation. Science 2010, 328, 1141−1144.
(29) Fu, Q.; Yang, F.; Bao, X. Interface-confined oxide nanostructures for catalytic oxidation reactions. Acc. Chem. Res. 2013, 46, 1692−1701.
(30) Yan, W.; Brown, S.; Pan, Z.; Mahurin, S. M.; Overbury, S. H.; Dai, S. Ultrastable gold nanocatalyst supported by nanosized non- oxide substrate. Angew. Chem., Int. Ed. 2006, 45, 3614−3618.
(31) Xiao, W.; Yang, S.; Zhang, P.; Li, P.; Wu, P.; Li, M.; Chen, N.; Jie, K.; Huang, C.; Zhang, N.; Dai, S. Facile synthesis of highly porous metal oxides by mechanochemical nanocasting. Chem. Mater. 2018, 30, 2924−2929.
(32) Liu, J.; Zhao, Z.; Xu, C.; Liu, J. Structure, synthesis, and catalytic properties of nanosize cerium-zirconium-based solid solutions in environmental catalysis. Chin. J. Catal. 2019, 40, 1438− 1487.
(33) Liu, J.-X.; Su, Y.; Filot, I. A. W.; Hensen, E. J. M. A linear scaling relation for CO oxidation on CeO_2-supported Pd. J. Am. Chem. Soc. 2018, 140, 4580−4587.
(34) Chen, G.; Zhao, Y.; Fu, G.; Duchesne, P. N.; Gu, L.; Zheng, Y.; Weng, X.; Chen, M.; Zhang, P.; Pao, C.-W.; Lee, J.-F.; Zheng, N. Interfacial effects in iron-nickel hydroxide−platinum nanoparticles enhance catalytic oxidation. Science 2014, 344, 495−499.
(35) Dong, J.; Fu, Q.; Jiang, Z.; Mei, B.; Bao, X. Carbide-supported Au catalysts for water−gas shift reactions: A new territory for the strong metal−support interaction effect. J. Am. Chem. Soc. 2018, 140, 13808−13816.
(36) Liu, J.; Cheng, H.; Bao, J.; Zhang, P.; Liu, M.; Leng, Y.; Zhang, Z.; Tao, R.; Liu, J.; Zhao, Z.; Dai, S. An aluminum hydroxide- mediated synthesis of mesoporous metal oxides by mechanochemical nanocasting strategy. J. Mater. Chem. A 2019, 7, 22977−22985.
(37) Machala, L.; Tuček, J.; Zbořil, R. Polymorphous transformations of nanometric iron (III) oxide: A review. Chem. Mater. 2011, 23, 3255−3272.
(38) Wang, X.; Maeda, N.; Baiker, A. Synergistic effects of Au and FeOx nanocomposites in catalytic NO reduction with CO. ACS Catal. 2016, 6, 7898−7906.
(39) Zhao, J.; Shu, Y.; Zhang, P. Solid-state CTAB-assisted synthesis of mesoporous Fe_3O_4 and Au@Fe_3O_4 by mechanochemistry. Chin. J. Catal. 2019, 40, 1078−1084.
(40) Wu, C. H.; Liu, C.; Su, D.; Xin, H. L.; Fang, H.-T.; Eren, B.; Zhang, S.; Murray, C. B.; Salmeron, M. B. Bimetallic synergy in cobalt−palladium nanocatalysts for CO oxidation. Nat. Catal. 2019, 2, 78−85.
(41) Yang, X.; Gao, Q.; Zhao, Z.; Guo, Y.; Guo, Y.; Wang, L.; Wang, Y.; Zhan, W. Surface tuning of noble metal doped perovskite oxide by synergistic effect of thermal treatment and acid etching: A new path to high-performance catalysts for methane combustion. Appl. Catal., B 2018, 239, 373−382.
(42) Whitford, C. L.; Stephenson, C. J.; Gomez-Gualdron, D. A.; Hupp, J. T.; Farha, O. K.; Snurr, R. Q.; Stair, P. C. Elucidating the nanoparticle−metal organic framework interface of Pt@ZIF-8 Catalysts. J. Phys. Chem. C 2017, 121, 25079−25091.
(43) Liu, X.; Liu, M.-H.; Luo, Y.-C.; Mou, C.-Y.; Lin, S. D.; Cheng, H.; Chen, J.-M.; Lee, J.-F.; Lin, T.-S. Strong metal−support interactions between gold nanoparticles and ZnO nanorods in CO oxidation. J. Am. Chem. Soc. 2012, 134, 10251−10258.
(44) Behafarid, F.; Ono, L. K.; Mostafa, S.; Croy, J. R.; Shafai, G.; Hong, S.; Rahman, T. S.; Bare, S. R.; Roldan Cuenya, B. Electronic properties and charge transfer phenomena in Pt nanoparticles on γ- Al_2O_3: Size, shape, support, and adsorbate effects. Phys. Chem. Chem. Phys. 2012, 14, 11766−11779.
(45) Lira, E.; Merte, L. R.; Behafarid, F.; Ono, L. K.; Zhang, L.; Roldan Cuenya, B. Role and evolution of nanoparticle structure and chemical state during the oxidation of NO over size- and shape- controlled Pt/γ-Al_2O_3 catalysts under operando conditions. ACS Catal. 2014, 4, 1875−1884.
(46) Wu, H.-C.; Chen, T.-C.; Chen, Y.-C.; Lee, J.-F.; Chen, C.-S. Formaldehyde oxidation on silica-supported Pt catalysts: The influence of thermal pretreatments on particle formation and on oxidation mechanism. J. Catal. 2017, 355,

87−100.
(47) Arnal, P. M.; Comotti, M.; Schüth, F. High-temperature-stable catalysts by hollow sphere encapsulation. Angew. Chem., Int. Ed. 2006, 45, 8224−8227.
(48) Belzunegui, J. P.; Sanz, J.; Rojo, J. M. Contribution of physical blocking and electronic effect to establishment of strong metal- support interaction in rhodium/titanium dioxide catalysts. J. Am. Chem. Soc. 1992, 114, 6749−6754.
(49) Ma, L.; Chen, X.; Li, J.; Chang, H.; Schwank, J. W. Electronic metal-support interactions in Pt/FeOx nanospheres for CO oxidation. Catal. Today 2019, DOI: 10.1016/j.cattod.2019.06.055.
(50) Hammer, B.; Hansen, L. B.; Nørskov, J. K. Improved adsorption energetics within density-functional theory using revised Perdew-Burke-Ernzerhof functionals. Phys. Rev. B: Condens. Matter 1999, 59, 7413−7421.
(51) Mason, S. E.; Grinberg, I.; Rappe, A. M. First-principles extrapolation method for accurate CO adsorption energies on metal surfaces. Phys. Rev. B: Condens. Matter 2004, 69, 161401.
(52) Guo, X.; Hoffman, A.; Yates, J. T., Jr. Adsorption kinetics and isotopic equilibration of oxygen adsorbed on the Pd (111) surface. J. Chem. Phys. 1989, 90, 5787−5792.
(53) Li, Q.; García-Muelas, R.; Lopez, N. Microkinetics of alcohol reforming for H_2 production from a FAIR density functional theory database. Nat. Commun. 2018, 9, 526.
(54) Liu, B.; Liu, J.; Li, T.; Zhao, Z.; Gong, X.-Q.; Chen, Y.; Duan, A.; Jiang, G.; Wei, Y. Interfacial effects of CeO_2-supported Pd nanorod in catalytic CO oxidation: A theoretical study. J. Phys. Chem. C 2015, 119, 12923−12934.

Supporting Information

Deep Understanding of Strong Metal Interface Confinement: A Journey of Pd/FeO_x catalysts

Jixing Liu[a,b,c,†], Lu Wang[b,†], Francis Okejiri[c], Jing Luo[a], Jiahua Zhao[e], Pengfei Zhang[e,*], Miaomiao Liu[c], Shize Yang[f], Zihao Zhang[c], Weiyu Song[b], Wenshuai Zhu[a], Jian Liu[b,*], Zhen Zhao[b], Guodong Feng[c,g,h,*], Chunming Xu[b], Sheng Dai[c,d,*]

[a] School of Chemistry and Chemical Engineering, Institution for Energy Research, Jiangsu University, Zhenjiang 212013, P. R. China;

[b] State Key Laboratory of Heavy Oil and Beijing Key Lab of Oil & Gas Pollution Control, China University of Petroleum, Beijing 102249, P. R. China;

[c] Department of Chemistry, University of Tennessee-Knoxville, Tennessee 37996-1600, United States;

[d] Chemical Sciences Division, Oak Ridge National Laboratory, Oak Ridge, Tennessee 37831, United States;

[e] School of Chemistry and Chemical Engineering, Shanghai Jiao Tong University, Shanghai 200240, P. R. China;

[f] Brookhaven National Laboratory, Upton, NY11973, United States;

[g] Ningbo Institute of Materials Technology and Engineering, Chinese Academy of Sciences, Ningbo, 315201, P. R. China;

[h] Key Laboratory of Advanced Molecular Engineering Materials, College of Chemistry and Chemical Engineering, Baoji University of Arts and Sciences, Baoji 721013, P. R. China.

*Correspondence and requests for materials should be addressed to P.F.Z. (E-mail: chemistryzpf@sjtu.edu.cn), J.L. (E-mail: liujian@cup.edu.cn), G.D.F. (E-mail: fengguodong00805@163.com), and S.D. (E-mail: dais@ornl.gov).

Computational details

To determine reaction pathways of catalytic oxidation of CO over Pd NPs and FeO_x/Pd NPs, all calculations were conducted using density functional theory (DFT) within the plane-wave pseudopotential as implemented in the VASP code with a cutoff energy of 450 eV.[1–3] The projector-augmented wave (PAW) method was used to represent the core-valence interaction.[4,5] The generalized gradient approximation (GGA) with the Perdew-Burke-Ernzerhof (PBE) exchange-correlation functional was used in the calculations.[6] To accurately treat the highly localized Fe3d-orbitals, we conducted spin-polarized DFT+U calculations with a value of U_{eff} = 3.0 eV applied to the Fe3d state.[7–11] The atomic positions were relaxed until the force on each atom was less than 0.05 eV/Å. Electronic energies were converged within 10^{-4} eV, which is accurate enough for the energy and geometry calculation. Transition state were searched using the Climbing Image Nudged Elastic Band approach.[12,13] Frequency analysis was carried out to ensure that there was only a single imaginary frequency for transition state. Adsorption energies have been calculated using the formula:

$$E_{ads} = E_{surf-X} - (E_{surf} + E_X)$$

Where E_{surf-X} is the total energy of the combined system (the adsorbate X bound to the substrate), E_{surf} is the energy of the substrate alone, and E_X is the total energy of the adsorbate in the gas phase.

To model the CO oxidation on a metal monophase, a five-layer ($2\sqrt{3} \times 5$) Pd (111) slab was used with 3 × 2 × 1 k-point sampling (**Figure S1a**). For FeO_x/Pd interface simulations, taking into account the lattice mismatch between FeO_x and Pd, a FeO_x ribbon covered Pd (111) slab model was applied with 3 × 2× 1 k-point sampling. The FeO_x ribbon consists of three Fe and three O columns with Fe atoms coordinated with the top layer of Pd substrate (**Figure S1b**). The bottom two layers of the Pd substrates were fixed, and the other atoms were all relaxed during the structural optimization. The vacuum gap thickness was set to 15 Å. Similar models have been successfully applied to study the catalytic activity of FeO_x/Pd.[3]

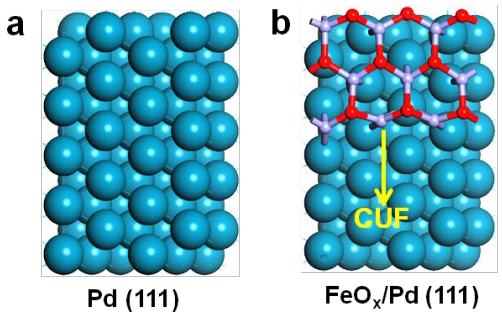

Figure S1. (a) five-layer ($2\sqrt{3} \times 5$) Pd (111) slab with 3 × 2 × 1 k-point sampling and (b) FeO_x ribbon covered Pd (111) slab model with 3 × 2× 1 k-point sampling.

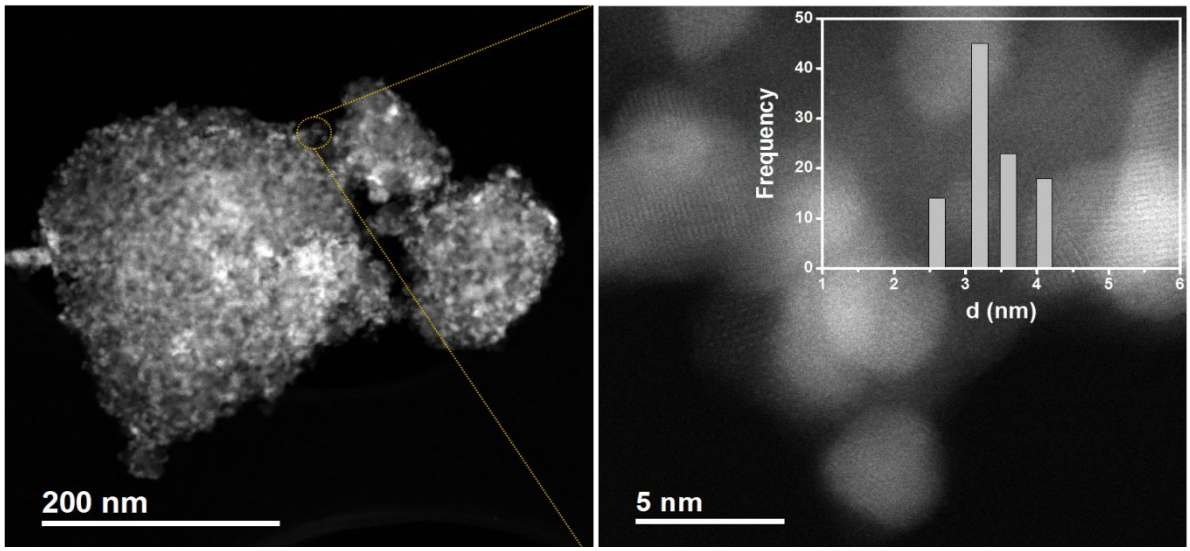

Figure S2. HAADF-STEM and high-resolution HAADF-STEM images of Fe_2O_3-loaded Pd NPs.

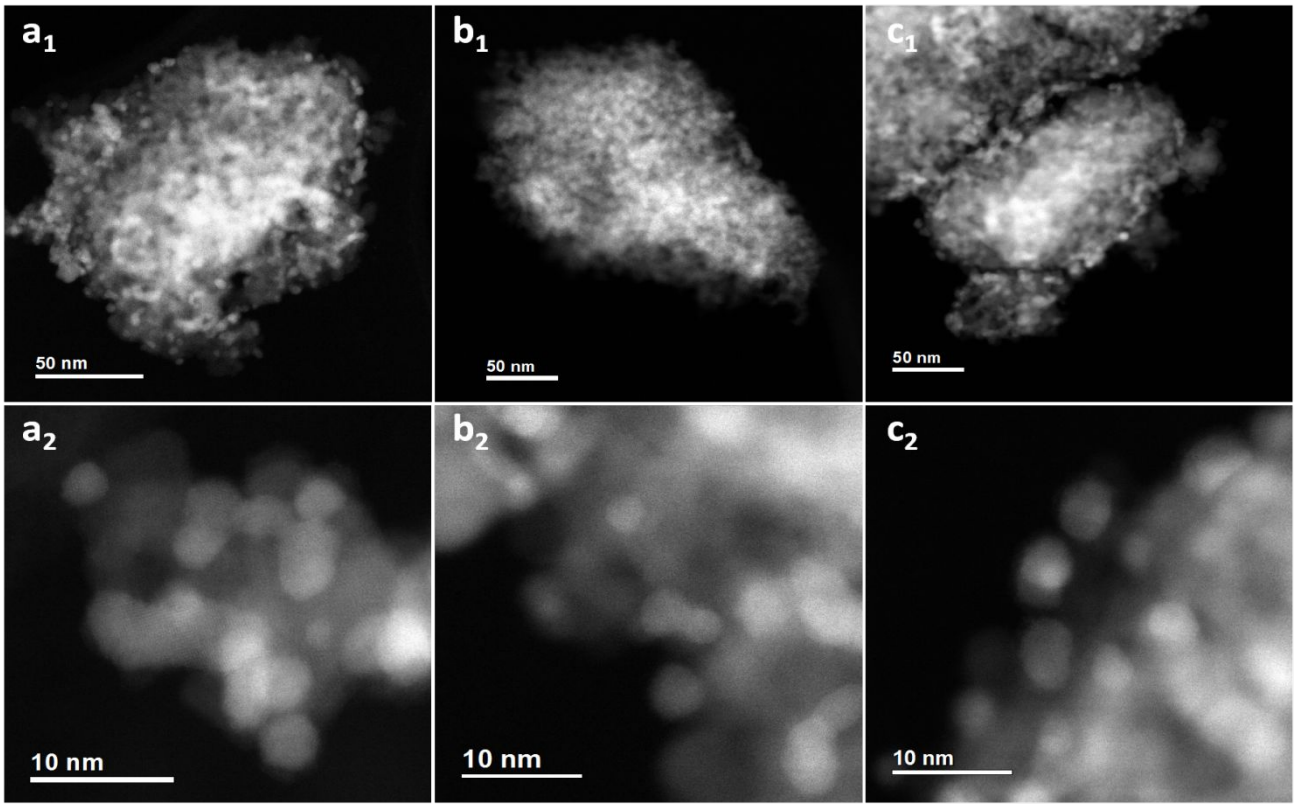

Figure S3. HAADF-STEM and high-resolution HAADF-STEM images of the catalysts: Pd/Fe_2O_3-air (**a_1**,**a_2**), Pd/Fe_2O_3-H_2-100 (**b_1**,**b_2**), and Pd/Fe_2O_3-H_2-400 (**c_1**,**c_2**).

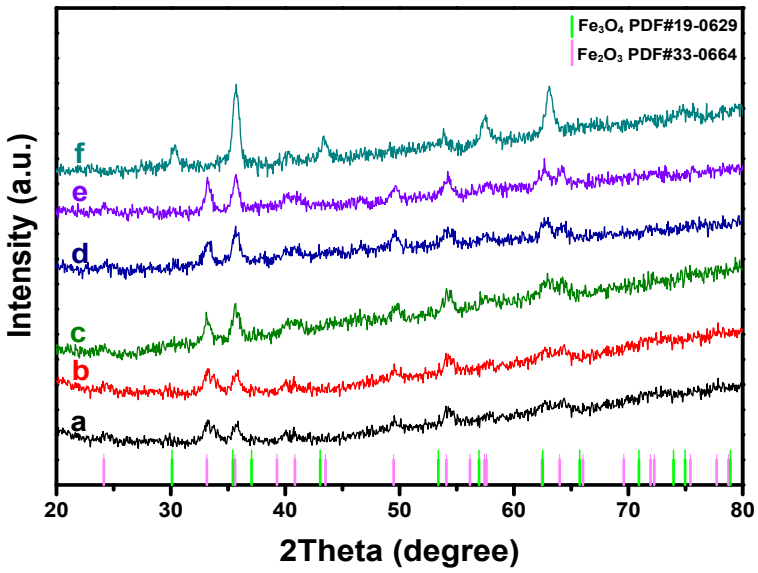

Figure S4. XRD patterns of the catalysts: **(a)** Fe_2O_3, **(b)** Pd/Fe_2O_3-air, **(c)** Pd/Fe_2O_3-H_2-50, **(d)** Pd/Fe_2O_3-H_2-100, **(e)** Pd/Fe_2O_3-H_2-200, and **(f)** Pd/Fe_2O_3-H_2-400.

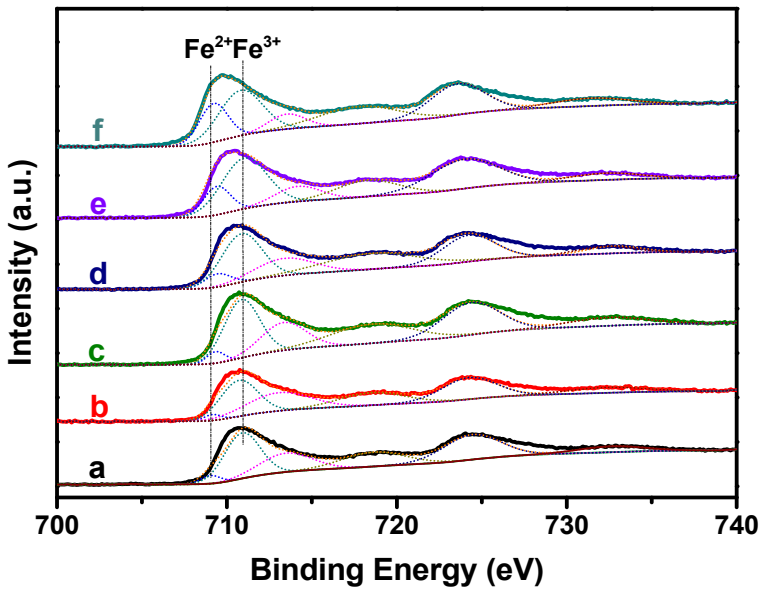

Figure S5. Fe2p XPS of the catalysts: (a) Fe_2O_3, (b) Pd/Fe_2O_3-air, (c) Pd/Fe_2O_3-H_2-50, (d) Pd/Fe_2O_3-H_2-100, (e) Pd/Fe_2O_3-H_2-200, and (f) Pd/Fe_2O_3-H_2-400.

Table S1 The surface relative concentration ratios of Fe obtained from the peak fitting of Fe2p XPS.

catalyst	surface relative concentration ratios		
	Fe^{2+}	Fe^{3+}	R^a
Fe_2O_3	0.092	0.908	90.8%
Pd/Fe_2O_3-air	0.086	0.914	91.4%
Pd/Fe_2O_3-H_2-50	0.095	0.905	90.5%
Pd/Fe_2O_3-H_2-100	0.154	0.846	84.6%
Pd/Fe_2O_3-H_2-200	0.255	0.745	74.5%
Pd/Fe_2O_3-H_2-400	0.425	0.575	57.5%

[a] The Fe species ratio of $Fe^{3+}/(Fe^{2+}+Fe^{3+})$.

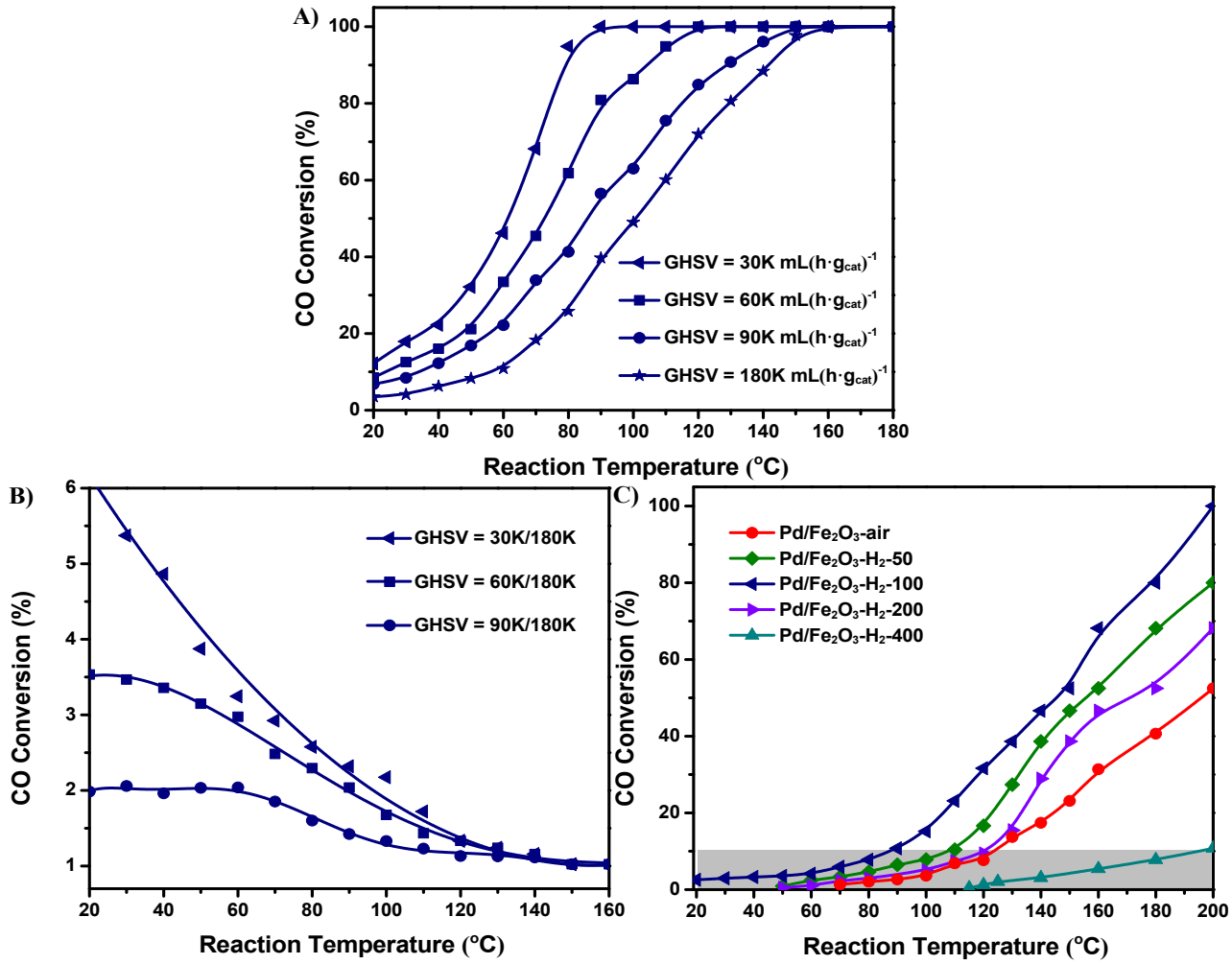

Figure S6. (A) CO conversions over Pd/Fe_2O_3-H_2-100 catalyst under different GHSVs; (B) CO conversion ratios with respect to that at GHSV = 180,000 $mL\cdot(h\cdot g_{cat})^{-1}$ as a function of reaction temperature, using data from (A); (C) CO conversion versus reaction temperature over Pd/Fe_2O_3 samples. The differential regime (CO conversion ≤ 10%) is marked grey. Reaction mixtures contain 1.0 volume % CO balanced with dry air. The feed gas rate: 20 mL/min and 3.3 mg of catalyst corresponding to GHSV of 360,000 $mL\cdot(h\cdot g_{cat})^{-1}$.

Firstly, CO oxidation was carried out at various GHSVs over Pd/Fe_2O_3-H_2-100 sample, and the results are displayed in **Figure S6A**, It was noted that increasing the GHSV from 30 to 180K $mL\cdot(h\cdot g_{cat})^{-1}$ resulted in the noticeable reduction of CO conversion through the whole tested temperature range. Secondly, Figure S6B presented CO conversion ratios with respect to that at GHSV = 180K $mL\cdot(h\cdot g_{cat})^{-1}$ as a function of reaction temperature using data from **Figure S6A**. It is well-known that CO conversion is expected to increase n-fold as the space velocity decreases n-fold in the absence of inter-particle mass transfer limitations. It was noted that, inter-particle mass-transfer limitation was more than 99% free under GHSV ≥ 180K $mL\cdot(h\cdot g_{cat})^{-1}$ condition. Thirdly, the ΔE_a for CO oxidation over Pd/Fe_2O_3 catalysts (**Figure 5B**) using reaction data were calculated under CO conversions less than 10% and displayed in Figure S6C.

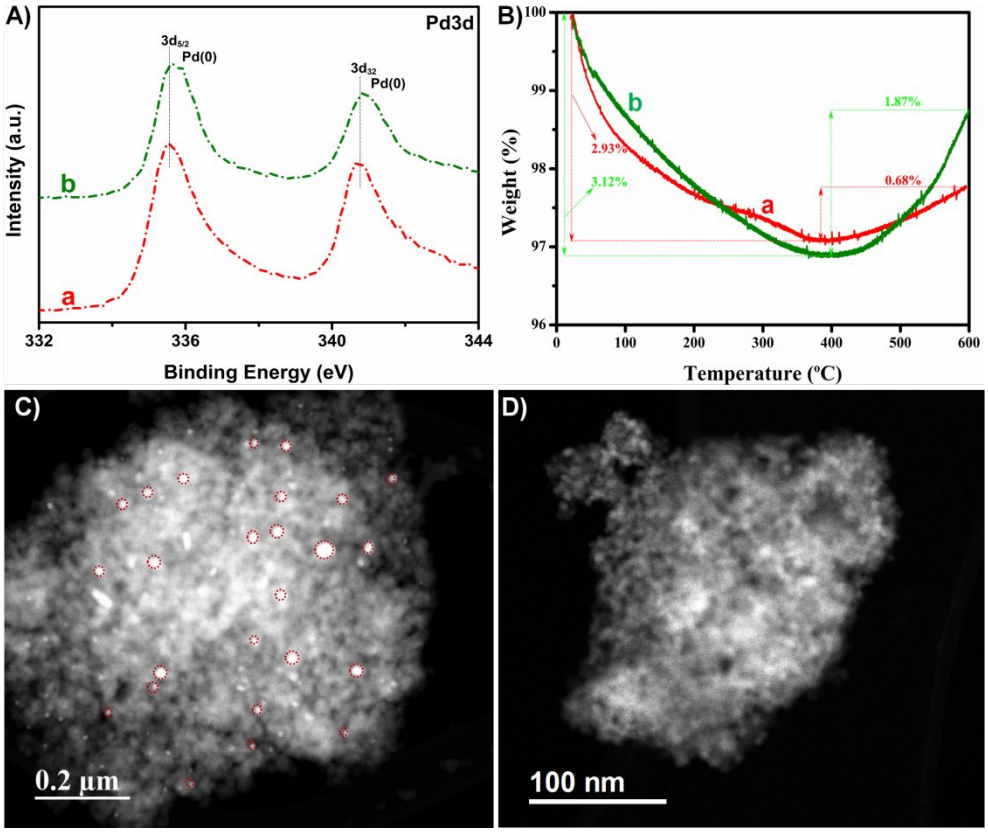

Figure S7. (A) Pd3d XPS and (B) TGA curves of spent (a) Pd/Fe_2O_3-air and (b) Pd/Fe_2O_3-H_2-100 catalysts after working at 150 °C for 24 h, HAADF-STEM images of spent (C) Pd/Fe_2O_3 and (D) Pd/Fe_2O_3-H_2-100 catalysts after working at 150 °C for 24 h.

Initially, XPS (**Figure S7A**) was carried out to analyze the variation of chemical valence of Pd in the Pd/Fe_2O_3-air and (b) Pd/Fe_2O_3-H_2-100 catalysts after working at 150 °C for 24 h. It was noted that no distinct position change for the both aged catalysts compared with the fresh ones, thus indicating that the deactivation of the Pd/Fe_2O_3-air catalyst should not be due to the oxidation of Pd NPs. Then the both aged catalysts were characterized by TGA (**Figure S7B**). Note that Pd/Fe_2O_3-air exhibited almost similar trend pattern with Pd/Fe_2O_3-H_2-100, and that the decreased weight should be both attributed to the loss water, rather than the buildup of carbonates covering the active sites. Finally, HAADF-STEM was conducted for the both spent catalysts to further probe the deactivation reason (**Figure S7C** and **S7D**). The results showed that the Pd NPs on Pd/Fe_2O_3-air occurred to sinter after working at 150 °C for 24 h. However, no obvious change was observed for Pd/Fe_2O_3-H_2-100 catalyst. Therefore, the above observations verified that the deactivation of the Pd/Fe_2O_3-air catalyst should be reasonable due to the loss of active sites resulting from the sintering of Pd NPs rather than the oxidation of Pd and the buildup of carbonates. It also demonstrated that the significantly improved stability of Pd/Fe_2O_3-H_2-100 could be attributed to the protection of outside FeO_x overlayers, which greatly inhibited the sintering of Pd NPs.

The Pd-only mechanism

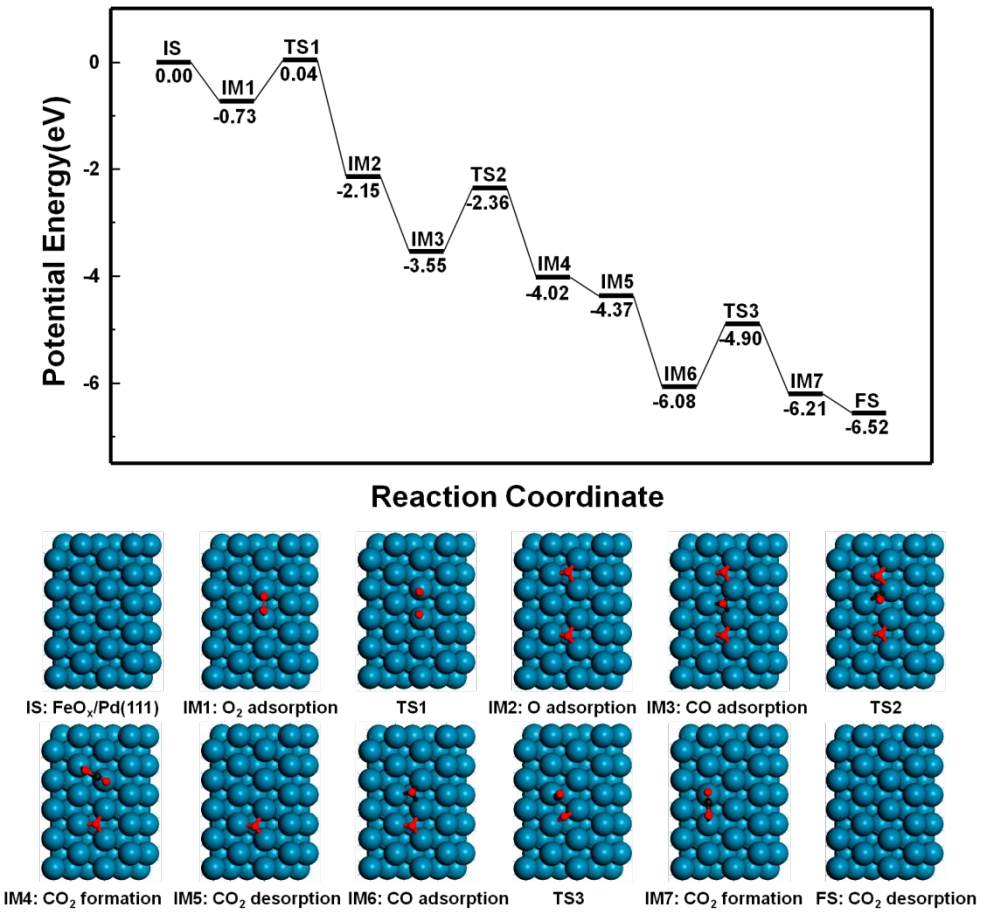

Figure S8. Potential energy diagram for the reaction of CO oxidation on the Pd (111) surface: The Pd-only mechanism (two dissociated O atoms absorbed on hcp hollow site).

1) Two O atoms absorbed on the fcc hollow site

The transition states, structures of intermediates, and potential energy diagram for CO oxidation over Pd (111) surface were calculated and depicted in **Figure S9**, which are similar with O atom adsorbed on the hcp hollow site. Firstly, O_2 bound to the bridge site of Pd-Pd atoms with adsorption energy of −0.73 eV (IM1). After undergoing a transition state (TS1) with an activation energy barrier of 0.77 eV, O_2 was split into two O atoms and adsorbed on the hcp hollow sites. The exothermic reaction energy of this step was 1.77 eV, which was increased by 0.35 eV compared with the adsorption of two O atoms on the hcp hollow site. It matches well with the 0.20 eV difference of the adsorption of single O atom. Then the CO molecule adsorbed on hollow site via C atom with adsorption energy of −1.42 eV (IM3). In addition, the CO molecule adsorbed on the fcc and hcp hollow sites was separately investigated, and no difference was found in their adsorption energies. The adsorbed CO thereafter combined with an adsorbed O atom on Pd to form CO_2 (IM4) with

exothermic reaction energy and activation barrier at 0.28 and 1.25 eV (TS2), respectively. Subsequently, CO_2 desorbed from IM4 state with exothermic reaction energy at 0.35 eV. Finally, another CO adsorbed on Pd (111) surface (IM6) followed by reacting with one O atom at surface with an activation barrier at 1.52 eV (TS3) to form CO_2 with an exothermic reaction energy at 0.04 eV (IM7), and the desorption of CO_2 was also exothermic by 0.28 eV (FS).

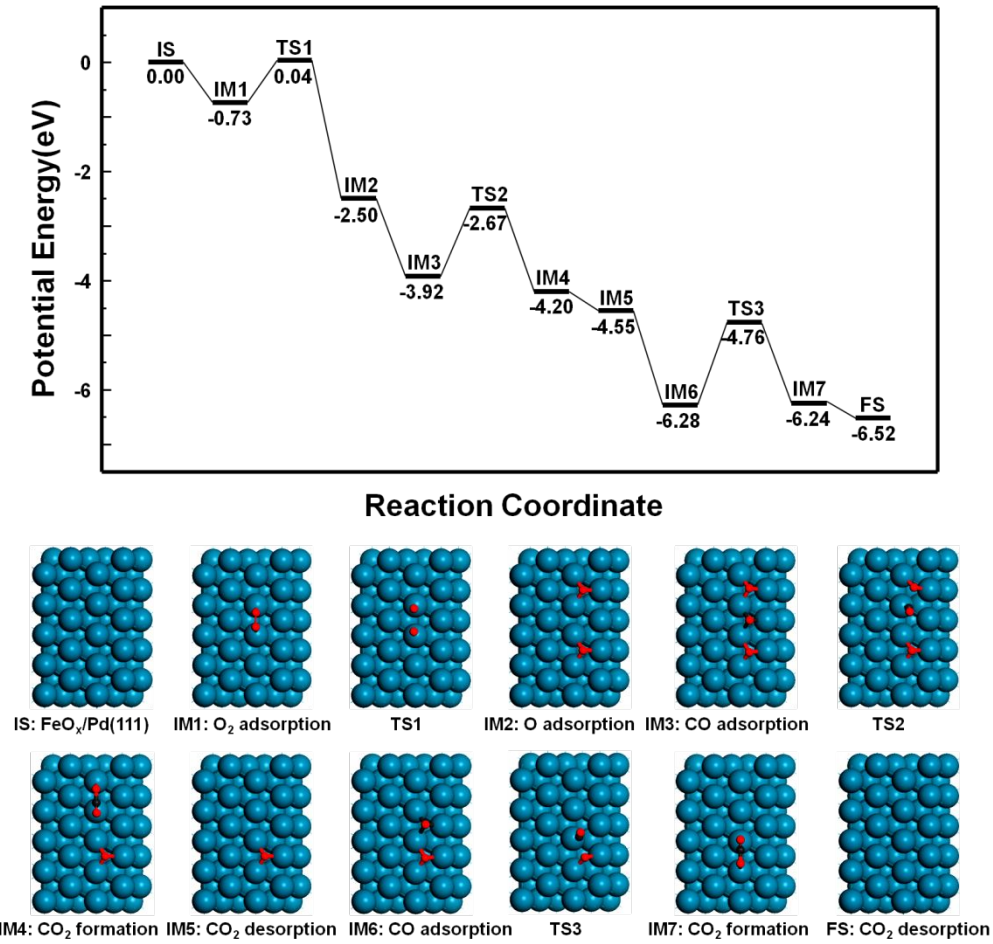

Figure S9. Potential energy diagram for the reaction of CO oxidation on the Pd (111) surface: The Pd-only mechanism (two dissociated O atoms absorbed on fcc hollow site).

2) Two O atoms adsorbed on hcp and fcc hollow sites, respectively

There are two different pathways when two atoms are adsorbed on the fcc and hcp hollow sites, respectively. The first pathway starts with the reaction of CO with O atoms adsorbed on the hcp hollow site, and the other path starts with the reaction of CO with O atoms adsorbed on the hcp hollow site. These two pathways are described as shown in **Figures S10** and **S11**, respectively. The O_2 molecules adsorbed on the Pd (111) surface were split into two O atoms by the transition state (TS1) and were adsorbed on the hcp and fcc hollow sites with an exothermic reaction energy at 1.57 eV (IM2), respectively. CO firstly reacted with the O atom adsorbed on the hcp hollow site and then

reacted with the O adsorbed on the fcc hollow site in **Figure S10**. The CO molecule was adsorbed on hollow site with adsorption energy at −1.51 eV (IM3). Then CO molecule would combine with the O atom adsorbed on the hcp hollow site to form CO_2 (IM4). This reaction step has an activation barrier at 1.12 eV and exothermic reaction energy at 0.39 eV. Subsequently, CO_2 desorbed from the surface with exothermic energy at 0.35 eV (IM5), and the next steps were similar to the pathway of CO reacting with the O two atoms absorbed on the fcc hollow sites.

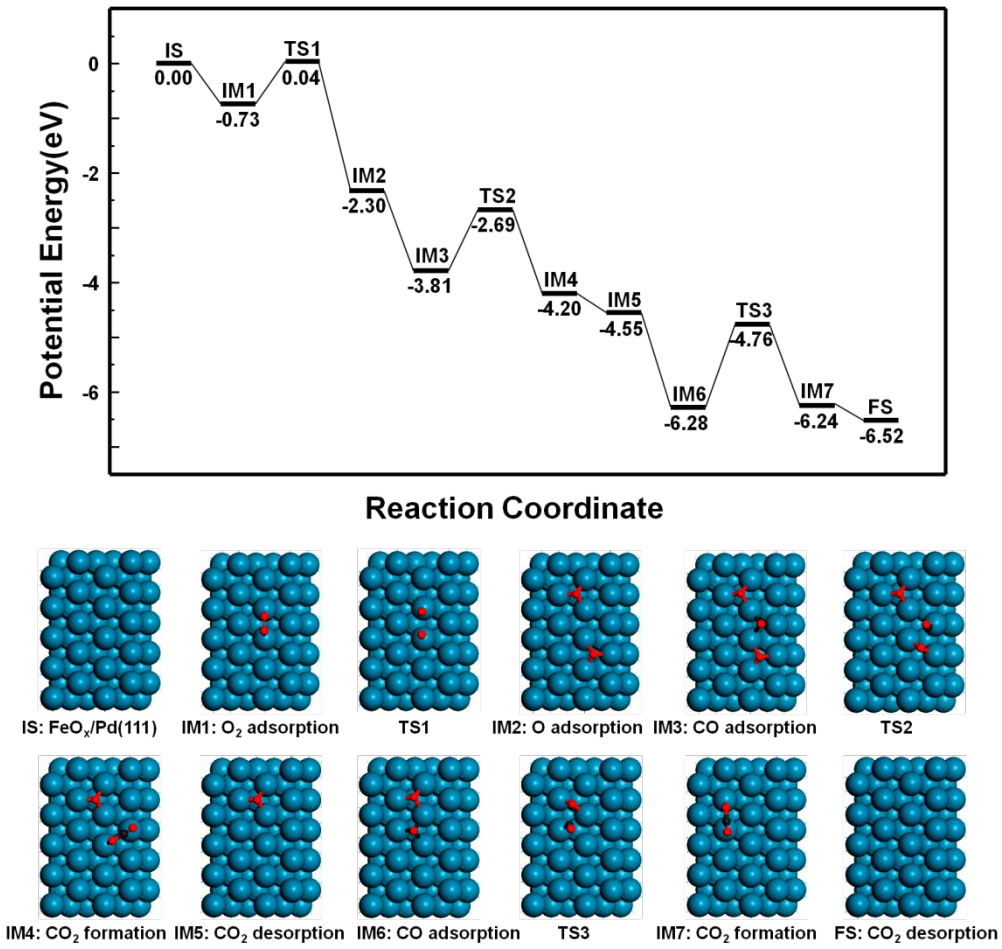

Figure S10. Potential energy diagram for the reaction of CO oxidation on the Pd (111) surface: The Pd-only mechanism (two dissociated O atoms absorbed on hcp and fcc hollow site, respectively. Start with O atom adsorbed on hcp hollow sites).

The reaction sequence of CO and O atoms in **Figure S11** is opposite to that in **Figure S10**. The CO was adsorbed on the Pd (111) surface (IM3) with exothermic energy at 1.54 eV, followed by reacting with the O atom absorbed on the fcc hollow site to produce CO_2 (IM4) with exothermic reaction energy and activation barrier (TS1) at 0.17 and 1.22 eV, respectively. Subsequently, CO_2 desorbed from the surface with exothermic reaction energy at 0.36 eV. The next steps were similar with the pathway of CO reacting with the O two atoms absorbed on the hcp hollow sites.

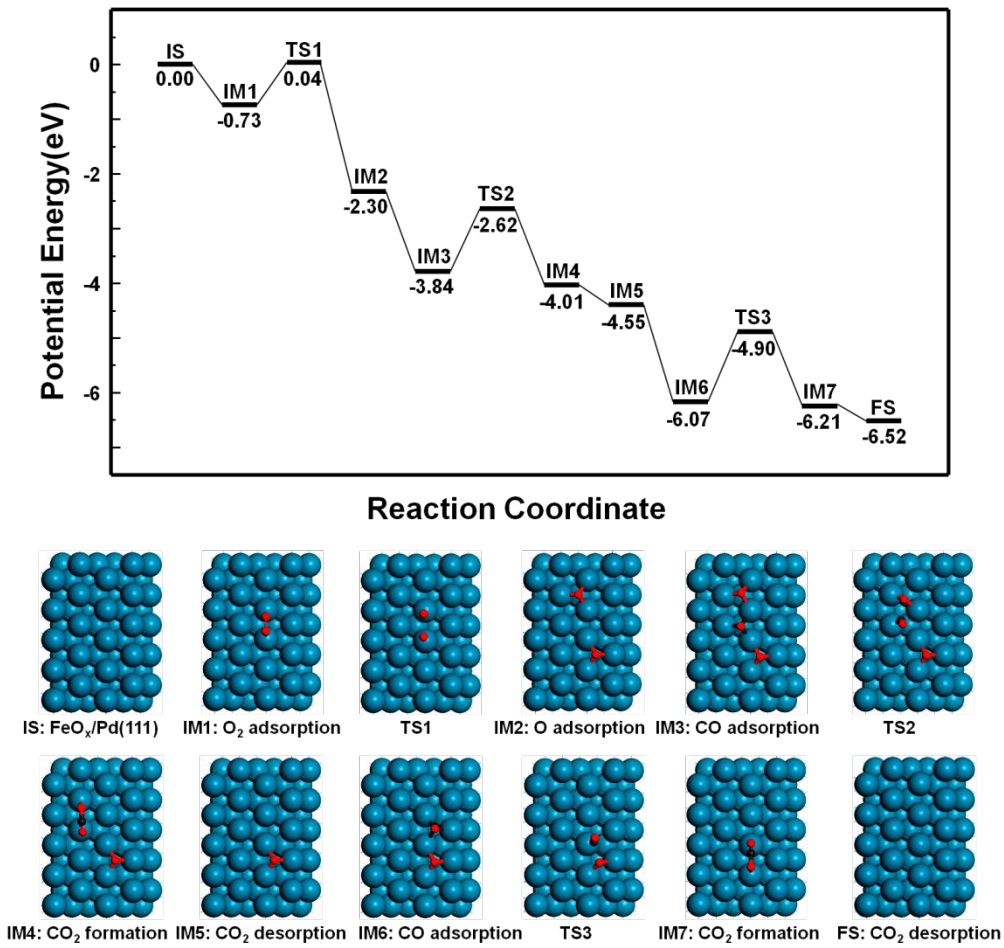

Figure S11. Potential energy diagram for the reaction of CO oxidation on the Pd (111) surface: The Pd-only mechanism (two dissociated O atoms absorbed on hcp and fcc hollow site, respectively. Start with O atom adsorbed on fcc hollow sites).

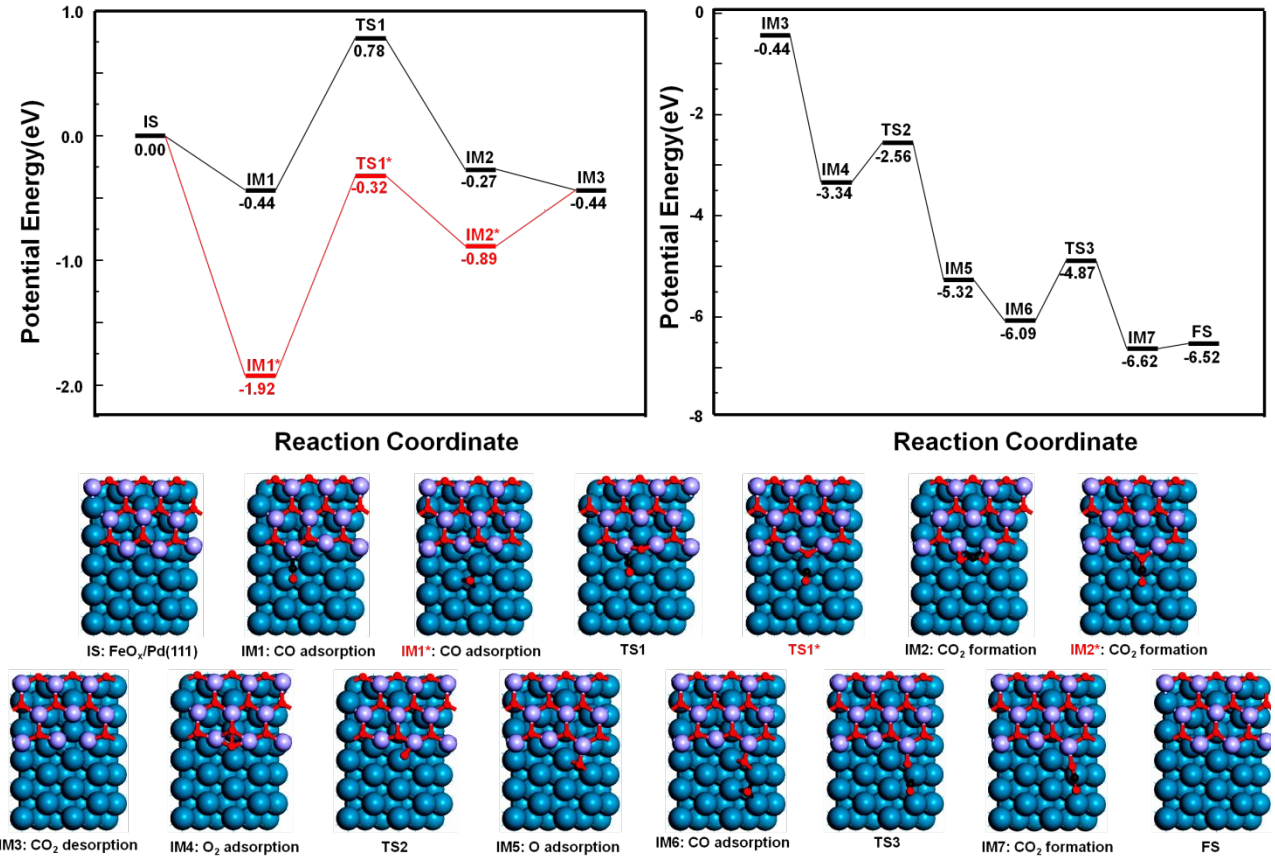

Figure S12. Potential energy diagram for the reaction of CO oxidation on the FeO_x/Pd (111) surface: M-vK mechanism.

REFERECES

1 Kresse, G.; Fürthmuller, J. Efficiency of ab-initio total energy calculations for metals and semiconductors using a plane-wave basis set. *Comput. Mater. Sci.* **1996**, *6*, 15−50.

2 Kresse, G.; Fürthmuller, J. Efficient iterative schemes for ab initio total-energy calculations using a plane-wave basis set. *Phys. Rev. B* **1996**, *54*, 11169−11186.

3 Chen, Z. Mao, Y.; Chen, J.; Wang, H.; Li, Y.; Hu, P. Understanding the dual active sites of the FeO/Pt (111) interface and reaction kinetics: Density functional theory study on methanol oxidation to formaldehyde. *ACS Catal.* **2017**, *7*, 4281−4290.

4 Kresse, G.; Joubert, D. From ultrasoft pseudopotentials to the projector augmented-wave method. *Phys. Rev. B* **1999**, *59*, 1758−1775.

5 Blöchl, P. E.; Jepsen, O.; Andersen, O. K. Improved tetrahedron method for brillouin-zone integrations. *Phys. Rev. B* **1994**, *49*, 16223−16233.

6 Perdew, J. P.; Burke, K.; Ernzerhof, M. Generalized gradient approximation made simple. *Phys. Rev. Lett.* **1996**, *77*, 3865−3868.

7 Anisimov, V. I.; Zaanen, J.; Andersen, O. K. Band theory and Mott insulators: Hubbard U instead of Stoner I. *Phys. Rev. B* **1991**, *44*, 943−954.

8 Anisimov, V. I.; Aryasetiawan, F.; Lichtenstein, A. I. First-principles calculations of the electronic structure and spectra of strongly correlated systems: the LDA+U method. *J. Phys. Condens. Matter.* **1997**, *9*, 767−808.

9 Fu, Q.; Li, W.-X.; Yao, Y.; Liu, H.; Su, H.-Y.; Ma, D.; Gu, X.-K.; Chen, L.; Wang, Z.; Zhang, H. Interface-confined ferrous centers for catalytic oxidation. *Science* **2010**, *328*, 1141−1144.

10 Prada, S.; Giordano, L.; Pacchioni, G.; Noguera, C.; Goniakowski, J. Properties of Pt-supported iron oxide ultra-thin films: Similarity of Hubbard-corrected and hybrid density functional theory description. *J. Chem. Phys.* **2014**, *141*, 144702−144709.

11 Spiridis, N. Phonons in ultrathin oxide films: 2D to 3D transition in FeO on Pt (111). *Phys. Rev. Lett.* **2015**, *115*, 186102.

12 Henkelman, G.; Uberuaga, B. P.; Jönsson, H. A climbing image nudged elastic band method for finding saddle points and minimum energy paths. *J. Chem. Phys.* **2000**, *113*, 9901–9904.

13 Henkelman, G.; Jönsson, H. Improved tangent estimate in the nudged elastic band method for finding minimum energy paths and saddle points. *J. Chem. Phys.* **2000**, *113*, 9978–9985.